SUPPLEMENTARY INFORMATION

Combining Electron Transfer, Spin Crossover, and Redox Properties in Metal-Organic Frameworks

Livia Getzner[1], Damian Paliwoda[1], Laure Vendier[1], Latévi Max Lawson-Daku[2], Aurelian Rotaru[3], Gábor Molnár[1], Saioa Cobo[1*] and Azzedine Bousseksou[1*]

[1] LCC, CNRS and Université de Toulouse, UPS, INP, Toulouse, France

[2] Faculté des Sciences – Université de Genève, 30 quai Ernest Ansermet, CH-1211 Genève 4, Suisse, Switzerland

[3] Department of Electrical Engineering and Computer Science & Research Center MANSiD, Stefan cel Mare University of Suceava, University St., No. 13, 720229 Suceava, Romania

Contents

1 Supplementary Methods

1.1 Synthesis of Ligands

1.1.1 Synthesis of 1-(2,4-Dinitrophenyl)-[4,4'-bipyridin]-1-ium chloride (di-NO_2-pbpyCl)

Dissolve 20 mmol (3.12 g) 4,4'-bipyridine and 20 mmol (4.05 g) 2,4-dinitrochlorobenzene in 50 ml acetone and stir at reflux for 12 h, cool, filter the precipitate that formed during reaction and wash multiple times with acetone. The beige powder **di-NO_2-pbpyCl** was obtained with 77 % yield.

^{1}H NMR (300 MHz, DMSO) δ 9.58 (d, *J* = 7.1 Hz, 2H), 9.16 (d, *J* = 2.5 Hz, 1H), 9.01 (dd, *J* = 8.7, 2.5 Hz, 1H), 8.98 – 8.92 (m, 4H), 8.46 (d, *J* = 8.7 Hz, 1H), 8.20 (d, *J* = 6.2 Hz, 2H). MS (ESI) m/z: Calc. for $[M]^+$ $C_{16}H_{11}N_4O_4$ 323.08. Found. 323.17.

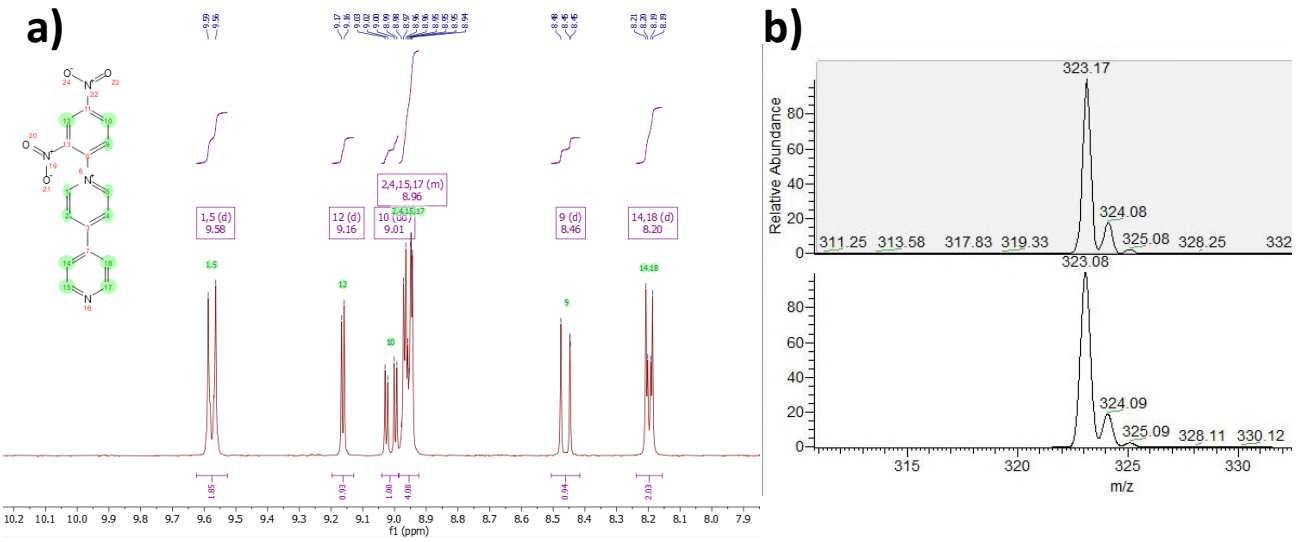

Supplementary Figure 1: (a) ^{1}H NMR and (b) ESI-MS spectra (experimental and calculated) of **di-NO_2-pbpy$^+$**.

1.1.2 Synthesis of 1-(4-Methylphenyl)-[4,4'-bipyridin]-1-ium chloride (CH_3-pbpyCl) (1)

Dissolve 2.75 mmol **di-NO_2-pbpyCl** (1.00 g) in 15 ml of ethanol abs. and add 8.25 mmol 4-methylaniline (0.88 g), reflux for 4 h, cool and add 20 ml dist. H_2O to remove byproduct as precipitate, evaporate all solvent and dissolve the crude product in as little methanol as possible, then precipitate **CH_3-pbpyCl** in diethyl ether and wash multiple times with diethylether to remove impurities. Light beige powder **CH_3-pbpyCl** was obtained with 91 % yield.

^{1}H NMR (400 MHz, DMSO) δ 9.48 (d, *J* = 7.0 Hz, 2H), 8.92 (d, *J* = 6.2 Hz, 2H), 8.78 (d, *J* = 7.1 Hz, 2H), 8.16 (d, *J* = 6.2 Hz, 2H), 7.83 (d, *J* = 8.5 Hz, 2H), 7.58 (d, *J* = 8.1 Hz, 2H), 2.47 (s, 3H). MS (ESI) m/z: Calc. for $[M]^+$ $C_{17}H_{15}N_2$ 247.12. Found. 247.17.

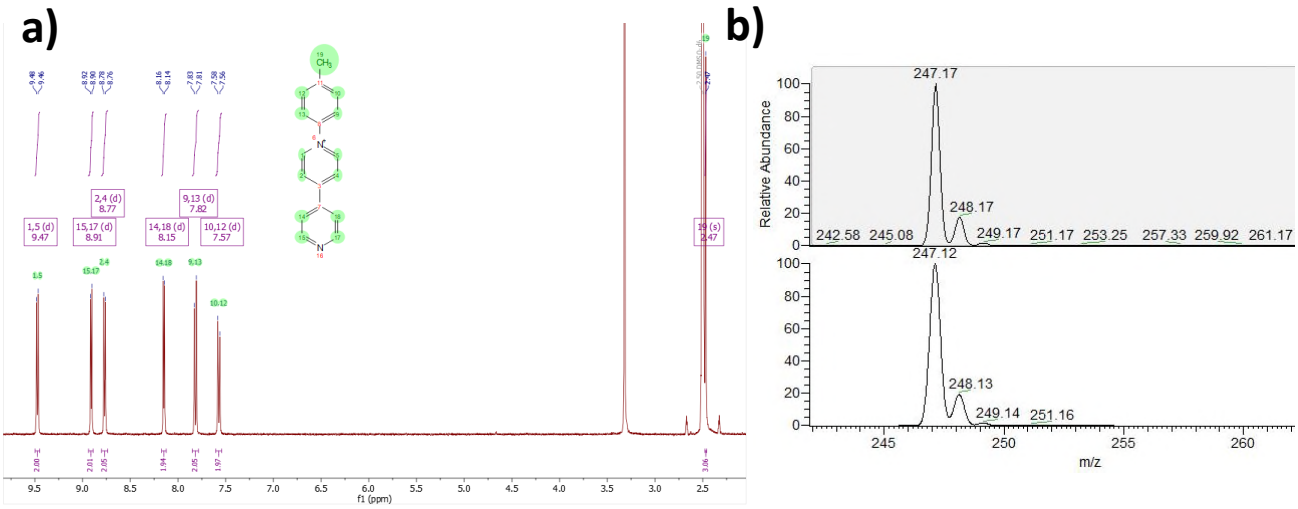

Supplementary Figure 2: (a) ^{1}H NMR and (b) ESI-MS spectra (experimental and calculated) of **CH_3-pbpy$^+$** (a).

1.1.3 Synthesis of 1-(4-Bromophenyl)-[4,4'-bipyridin]-1-ium chloride (Br-pbpyCl) (2)

Dissolve 3 mmol **di-NO_2-pbpyCl** (1.07 g) in 15 ml of ethanol abs. and add 9 mmol 4-bromoaniline (1.55 g), reflux for 4 h, cool and add 20 ml dist. H_2O to remove byproduct as precipitate, evaporate all solvent and dissolve crude product in as little methanol as possible, then precipitate **Br- pbpyCl** in diethyl ether and wash multiple times with diethylether to remove impurities. Light beige powder **Br- pbpyCl** was obtained with 93 % yield.

^{1}H NMR (400 MHz, DMSO) δ 9.48 (d, *J* = 7.0 Hz, 2H), 8.91 (d, *J* = 6.2 Hz, 2H), 8.79 (d, *J* = 7.1 Hz, 2H), 8.15 (d, *J* = 6.2 Hz, 2H), 8.00 (d, *J* = 8.5 Hz, 2H), 7.90 (d, *J* = 8.1 Hz, 2H). MS (ESI) m/z: Calc. for $[M]^+$ $C_{16}H_{12}N_2Br$ 311.02 Found.311.17.

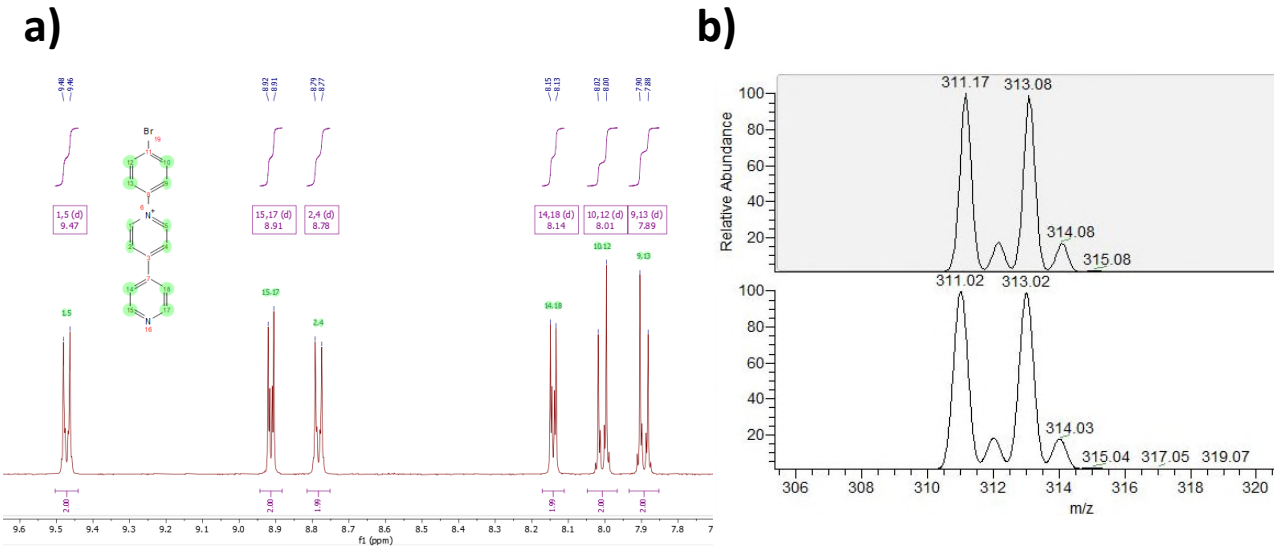

Supplementary Figure 3: (a) ^{1}H NMR and (b) ESI-MS spectra (experimental and calculated) of **Br-pbpy$^+$** (a).

1.1.4 Synthesis of 1-(Methyl-4-aminobenzoate)-[4,4'-bipyridin]-1-ium chloride ($COOCH_3$-pbpyCl) (3)

Dissolve 1.1 mmol **di-NO_2-pbpyCl** (0.40 g) in 10 ml of ethanol abs. and add 3.3 mmol methyl-4-aminobenzoate (0.51 g) and 300 µL triethylamine reflux for 4 h, cool and add 20 ml dist. H_2O to remove byproduct as precipitate, evaporate all solvent and dissolve crude product in as little methanol as possible, then precipitate **$COOCH_3$-pbpyCl** in diethyl ether and wash multiple times with diethylether to remove impurities. Light yellow powder **$COOCH_3$-pbpyCl** was obtained with 66 % yield.

^{1}H NMR (300 MHz, DMSO) δ 9.55 (d, *J* = 7.1 Hz, 2H), 8.92 (d, *J* = 6.2 Hz, 2H), 8.83 (d, *J* = 7.1 Hz, 2H), 8.31 (d, *J* = 8.8 Hz, 2H), 8.17 (d, *J* = 6.3 Hz, 2H), 8.09 (d, *J* = 8.8 Hz, 2H), 3.95 (s, 3H). MS (ESI) m/z: Calc. for $[M]^+$ $C_{18}H_{15}N_2O_2$ 291.11. Found.291.25.

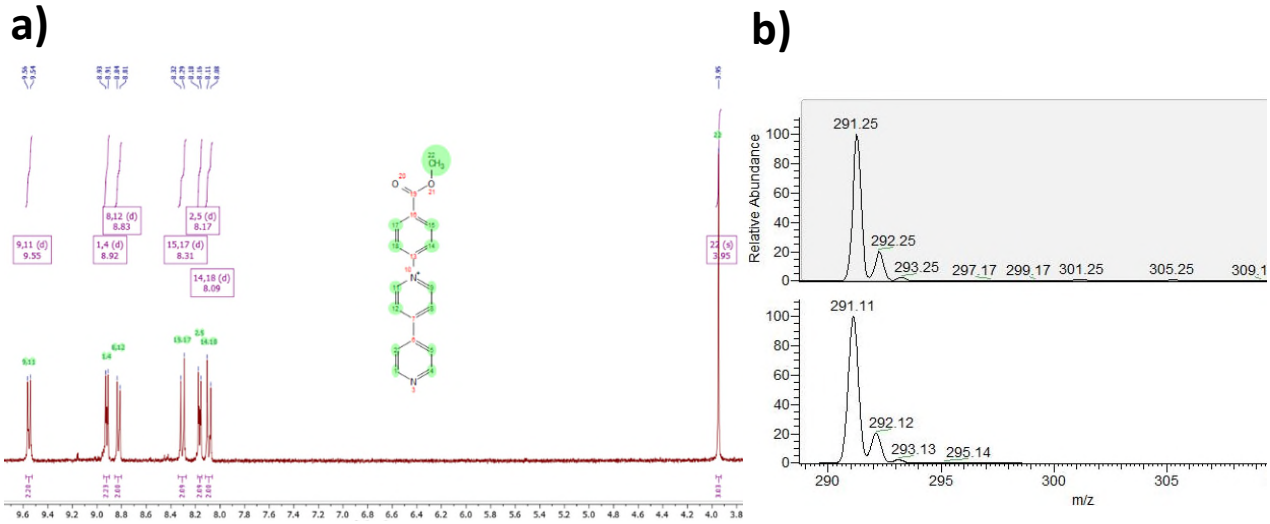

Supplementary Figure 4: (a) ^{1}H NMR and (b) ESI-MS spectra (experimental and calculated) of **$COOCH_3$-pbpy$^+$**.

1.1.5 Synthesis of 1-(4-Nitrophenyl)-[4,4'-bipyridin]-1-ium chloride (NO_2-pbpyCl) (4)

Dissolve 1.0 mmol **di-NO_2-pbpyCl** (0.36 g) in 10 ml of ethanol abs. and add 3 mmol 4-nitroaniline (0.41 g), reflux for 24 h, cool and add 20 ml dist. H_2O to remove byproduct as precipitate, evaporate all solvent and dissolve crude product in as little methanol as possible, then precipitate **NO_2-pbpyCl** in tetrahydrofuran (THF) and wash multiple times with THF to remove impurities. Yellow powder **NO_2-pbpyCl** was obtained with 60 % yield.

1H NMR (300 MHz, DMSO) δ 9.58 (d, J = 7.1 Hz, 2H), 8.94 (d, J = 6.2 Hz, 2H), 8.86 (d, J = 7.1 Hz, 2H), 8.62 (d, J = 9.1 Hz, 2H), 8.24 (d, J = 9.1 Hz, 2H), 8.18 (d, J = 6.2 Hz, 2H). MS (ESI) m/z: Calc. for $[M]^+$ $C_{16}H_{12}N_3O_2$ 278.09 Found.278.17.

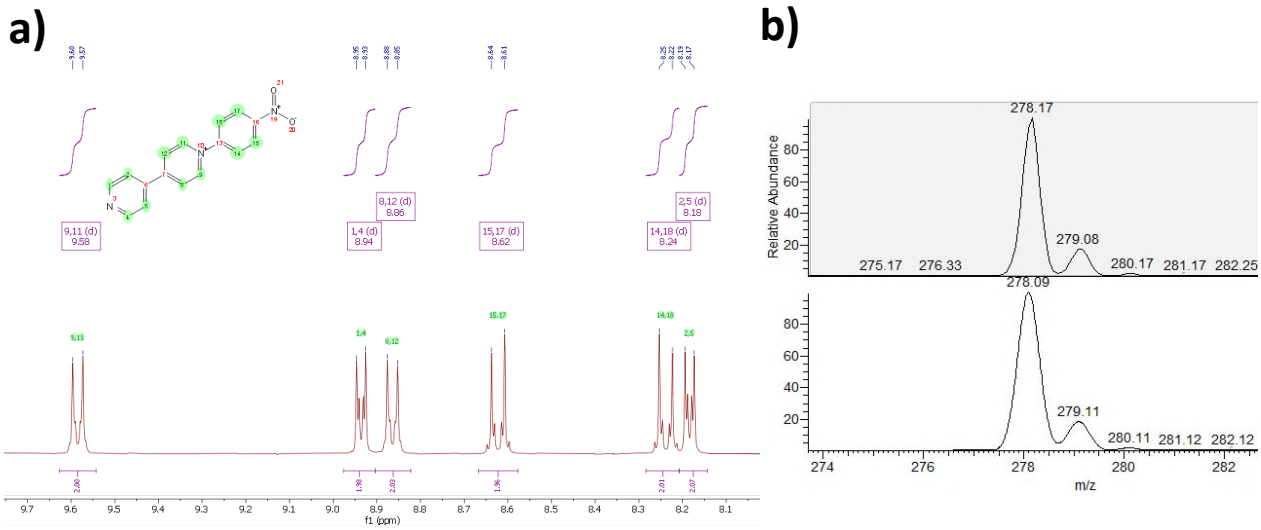

Supplementary Figure 5: (a) ^{1}H NMR and (b) ESI-MS spectra (experimental and calculated) of **NO_2-pbpy$^+$**.

1.2 Synthesis of clathrates {$Fe(L)_2[\mu_2\text{-}M(CN)_4]_2 \cdot xH_2O$} as powders (L= CH_3-pbpy$^+$, $COOCH_3$-pbpy$^+$, NO_2-pbpy$^+$or Br-pbpy$^+$; M= Ni or Pt)

0.5 mmol of the respective ligand (L= CH_3-pbpyCl, $COOCH_3$-pbpyCl, NO_2-pbpyCl or Br-pbpyCl) are dissolved in 10 mL 50/50 v% EtOH / H_2O dist., then 0.25 mmol of $Fe(BF_4)_2 \cdot 6\ H_2O$ are added with a small amount of ascorbic acid. Once dissolved, 0.5 mmol of $K_2[Ni(CN)_4] \cdot x\ H_2O$ or $K_2[Pt(CN)_4]$ are added and purple precipitates form immediately. The mixture is stirred for 1 h, filtered and the precipitate is washed several times with EtOH / H_2O dist., then dried in the oven.

All clathrates were analysed by ICP-OES to determine their respective Fe and Ni content. In addition, CHN analyses of all clathrates were carried out to determine their respective C, N, H content.

1a) {Fe(**CH_3-pbpy$^+$**)$_2$[$Ni(CN)_4$]$_2 \cdot 2H_2O$} : Theory: Fe 6.1 %, Ni 12.9 %, C 55.3 %, H 3.8 %, N 18.4 %. Found: Fe 6.0 %, Ni 13.7 %, C 54.0%, H 3.0 %, N 18.0 %.

1b) {Fe(**CH_3-pbpy$^+$**)$_2$[$Pt(CN)_4$]$_2 \cdot 2H_2O$} : Theory: Fe 4.7 %, Pt 32.9 %, C 42.6 %, H 2.9 %, N 14.2 %. Found: Fe 4.3 %, Pt 31.9 %, C 42.4 %, H 2.2 %, N 14.1 %.

2a) {Fe(**Br-pbpy$^+$**)$_2$[$Ni(CN)_4$]$_2 \cdot 2H_2O$} : Theory: Fe 5.4 %, Ni 11.3 %, C 46.1 %, H 2.7 %, N 16.1 %. Found: Fe 5.3 %, Ni 12.1 %, C 44.8 %, H 3.0 %, N 15.8 %.

2b) {Fe(**Br-pbpy$^+$**)$_2$[$Pt(CN)_4$]$_2 \cdot 2H_2O$} : Theory: Fe 4.3 %, Pt 29.7 %, C 36.6 %, H 2.2 %, N 12.8 %. Found: Fe 4.3 %, Pt 30.5 %, C 35.8 %, H 1.2 %, N 12.5 %.

3a) {Fe(**$COOCH_3$-pbpy$^+$**)$_2$[$Ni(CN)_4$]$_2 \cdot 2H_2O$} : Theory: Fe 5.6 %, Ni 11.7 %, C 52.8 %, H 3.4 %, N 16.8 %. Found: Fe 5.3 %, Ni 13.0 %, C 49.7 %, H 2.7 %, N 16.6 %.

3b) {Fe(**$COOCH_3$-pbpy$^+$**)$_2$[$Pt(CN)_4$]$_2 \cdot 2H_2O$} : Theory: Fe 4.4 %, Pt 30.6 %, C 41.5 %, H 2.7 %, N 13.2 %. Found: Fe 4.1 %, Pt 28.8 %, C 41.2 %, H 1.7 %, N 13.1 %.

4a) {Fe(**NO_2-pbpy$^+$**)$_2$[$Ni(CN)_4$]$_2 \cdot 2H_2O$} : Theory: Fe 5.7 %, Ni 12.1 %, C 49.3 %, H 2.9 %, N 20.1 %. Found: Fe 6.0 %, Ni 14.5 %, C 47.1 %, H 2 %, N 19.9 %.

4b) {Fe(**NO_2-pbpy$^+$**)$_2$[$Pt(CN)_4$]$_2 \cdot 2H_2O$} : Theory: Fe 4.5 %, Pt 31.3 %, C 38.5 %, H 2.3 %, N 15.7 %. Found: Fe 5.1 %, Pt 30.9 %, C 34.2 %, H 1.2 %, N 15.3 %.

The theoretical values are obtained from the crystal structures. Compounds 4a and 4b show the lowest crystallinity in pXRD measurements (see SI section 3.3), the defects of the structure could explain the higher than expected Ni content for those clathrates. Moreover, as the compounds are insoluble, the ICP analyses were done after mineralization in aqua regia, where, however, it is difficult to ensure complete dissolution. This could explain the slight inconsistencies observed.

1.3 Synthesis of clathrates {$Fe(L)_2[\mu_2\text{-}Pt(CN)_4]_2 \cdot xH_2O$ } as crystals (L= CH_3-pbpy$^+$, $COOCH_3$-pbpy$^+$ or Br-pbpy$^+$)

0.35 mmol of the respective ligand (L= **CH_3-pbpyCl, $COOCH_3$-pbpyCl or Br-pbpyCl**) are dissolved in 8 mL 50/50 v% EtOH / H_2O dist. and filled into an H-tube, then 0.1 mmol of $Fe(BF_4)_2 \cdot 6\ H_2O$ in 0.5 mL 50/50 v% EtOH / H_2O dist. are added on one side and 0.2 mmol of $K_2[Pt(CN)_4]$ in 0.5 mL 50/50 v% EtOH / H_2O dist. are added on the other side. After several days/weeks red crystals are formed and characterized via single crystal XRD.

2 Supplementary Figures
2.1 Electrochemical studies

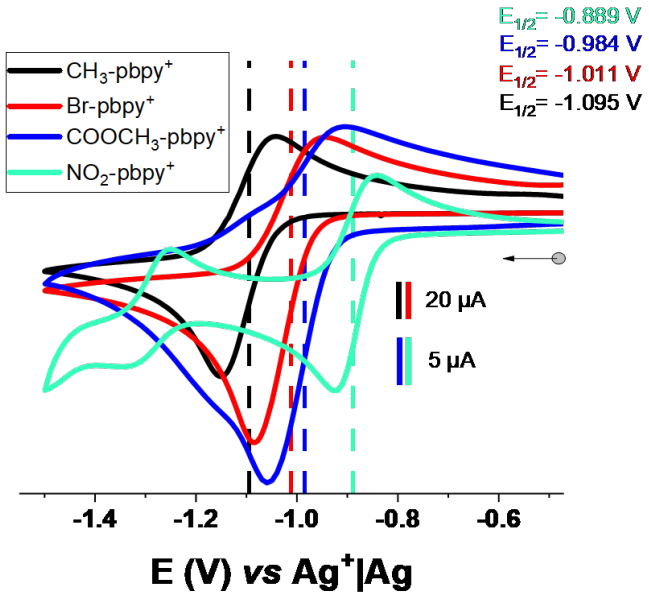

Supplementary Figure 6: Cyclic voltammetry of **CH_3-pbpy$^+$** (black), **Br-pbpy$^+$** (red), **$COOCH_3$-pbpy$^+$** (blue) and **NO_2-pbpy$^+$** (green, the second wave is attributed to the reduction of the NO_2 moiety) showing the quasi-reversible reduction of the bipyridinium unit. [C]= 10^{-4} M in 0.1M TBAP/CH_3CN, reference: $Ag^+|Ag$ electrode ([Ag^+]=10^{-2} M in CH_3CN); Scan rate: 100 mV·s^{-1}).

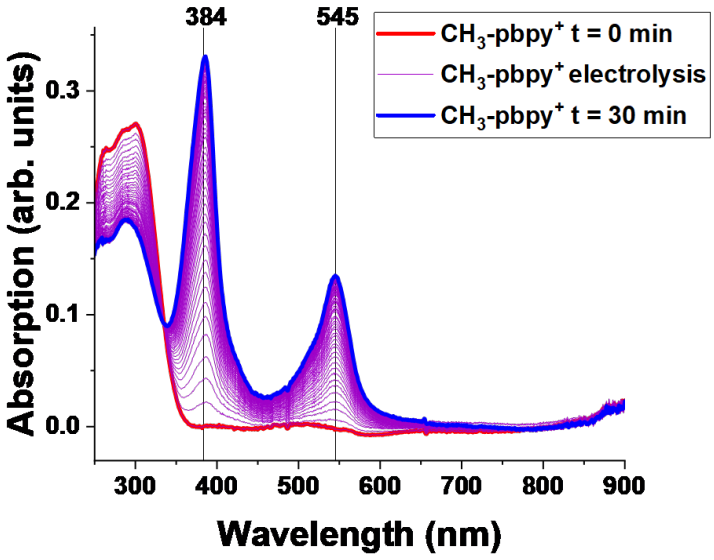

Supplementary Figure 7: Evolution of the UV-vis absorption spectra during the electrolysis of **CH_3-pbpy$^+$** at E_{app}=−1.2 V (initial state, red line), spectra taken every 30 seconds ([C]=0.1 mM in 0.1 M TBAP/CH_3CN, v: 100 mV·s^{-1}, VC, Ø=3 mm, E (V) *vs* Ag^+/Ag 10^{-2} M in CH_3CN).

2.2 Magnetic and optical behavior

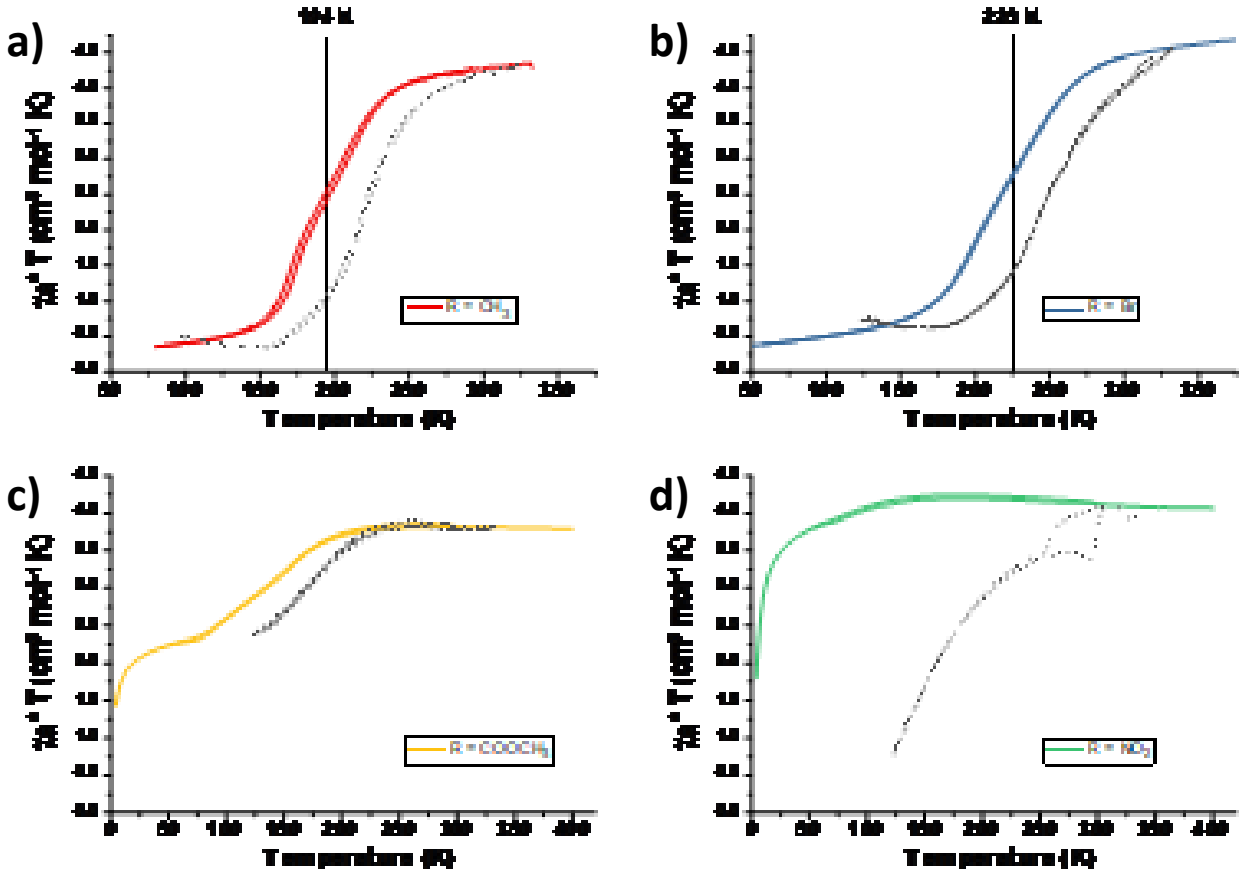

Supplementary Figure 8: $\chi_a T$ *vs* T (χ_a stands for the molar magnetic susceptibility) and variable temperature optical reflectivity for samples of **1-4b** {Fe(**R-pbpy**$^+$)$_2$[Pt(CN)$_4$]$_2$·2H$_2$O} (R= CH_3, (curve a; red), Br (curve b; blue), $COOCH_3$ (curve c ;yellow) and NO_2 (curve d; green). The magnetic measurements are shown in the respective colors, the corresponding optical reflectivity curves in grey dots. While a slight shift of the SCO temperature can be seen, the materials general behavior is comparable to the respective Ni compounds shown in the manuscript.

2.3 PRDX

The powder X-ray diffraction (XRD) analyzes were carried out at room temperature on a Rigaku Miniflex600 benchtop powder diffractometer in a theta/2 theta geometry using a Cu anode (K-Alpha1 [Å] 1.54060), a fast 1D detector with energy selection, and a 6-position sample changer. Samples were measured in a range of 2theta from 5 to 60°, every 0.02°, with a speed of 5° per minute. Powder diffraction data obtained from samples of {Fe(**R-pbpy**$^+$)$_2$[μ$_2$-Ni(CN)$_4$]$_2$· 2H$_2$O} is refined using unit cell parameters of the Pt analogue. As there is a large difference between these two metals there are small discrepancies regarding unit cell parameters, however, the fit is good enough to reason that both compounds show the same structural arrangement.

a)

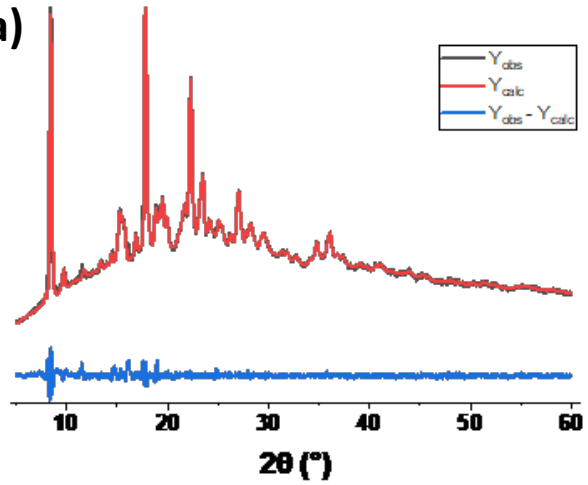

b)

	{Fe(**CH$_3$-pbpy**$^+$)$_2$[μ$_2$-Ni(CN)$_4$]$_2$ · 2H$_2$O} refined unit cell data (pXRD)	{Fe(**CH$_3$-pbpy**$^+$)$_2$[μ$_2$-Pt(CN)$_4$]$_2$ · 2H$_2$O} single crystal unit cell data
a (Å)	21.0409	20.7193
b (Å)	13.1553	13.2689
c (Å)	15.8080	15.7569
α (°)	90	90
β (°)	90.653	92.253
γ (°)	90	90

Supplementary Figure 9: a) pXRD diffractogram of {Fe(**CH$_3$-pbpy**$^+$)$_2$[μ$_2$-Ni(CN)$_4$]$_2$ · 2H$_2$O} (GOF= 1.71, Rp= 1.24, wRp= 2.10) and (b) obtained unit cell parameters via refinement using single crystal data of the Pt analogue.

a)

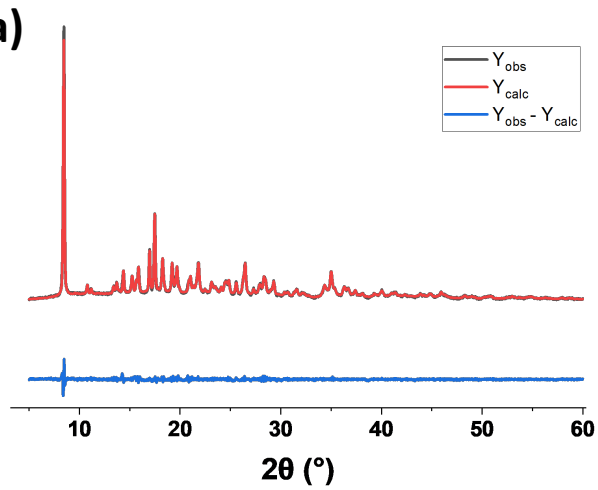

b)

	{Fe(**CH$_3$-pbpy**$^+$)$_2$[μ$_2$-Pt(CN)$_4$]$_2$ · 2H$_2$O} refined unit cell data (pXRD)	{Fe(**CH$_3$-pbpy**$^+$)$_2$[μ$_2$-Pt(CN)$_4$]$_2$ · 2H$_2$O} single crystal unit cell data
a (Å)	20.8827	20.7193
b (Å)	13.2213	13.2689
c (Å)	15.7897	15.7569
α (°)	90	90
β (°)	92.816	92.253
γ (°)	90	90

Supplementary Figure 10: a) pXRD diffractogram of {Fe(**CH$_3$-pbpy**$^+$)$_2$[μ$_2$-Pt(CN)$_4$]$_2$ · 2H$_2$O} (GOF= 0.99, Rp= 3.37, wRp= 4.44) and (b) obtained unit cell parameters via refinement using the corresponding single crystal data.

a)

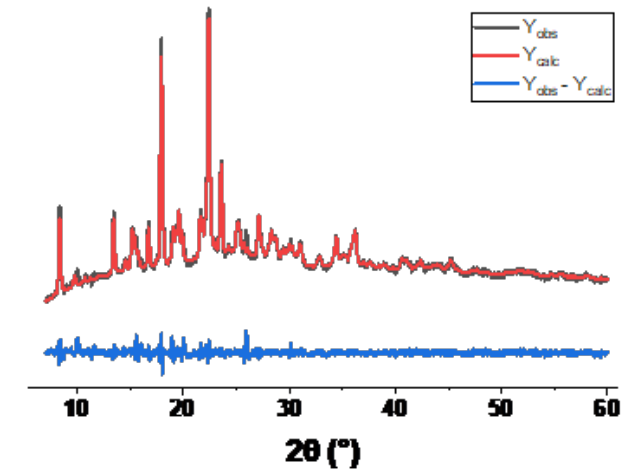

b)

	{Fe(**Br-pbpy**$^+$)$_2$[μ$_2$-Ni(CN)$_4$]$_2$ · 2H$_2$O} refined unit cell data (pXRD)	{Fe(**Br-pbpy**$^+$)$_2$[μ$_2$-Pt(CN)$_4$]$_2$ · 2H$_2$O} single crystal unit cell data
a (Å)	21.1976	21.2590
b (Å)	13.1744	12.9694
c (Å)	15.8027	15.4095
α (°)	90	90
β (°)	92.657	92.8110
γ (°)	90	90

Supplementary Figure 11: a) pXRD diffractogram of {Fe(**Br-pbpy**$^+$)$_2$[Ni(CN)$_4$]$_2$·2H$_2$O} (GOF= 1.41, Rp= 1.92, wRp= 2.92) and (b) obtained unit cell parameters via refinement using single crystal data of the Pt analogue.

a)

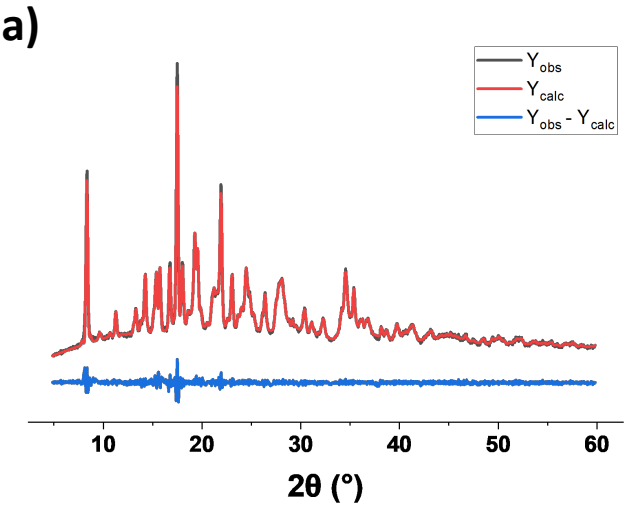

b)

	{Fe(**Br-pbpy**$^+$)$_2$[μ$_2$-Pt(CN)$_4$]$_2$ · 2H$_2$O} refined unit cell data (pXRD)	{Fe(**Br-pbpy**$^+$)$_2$[μ$_2$-Pt(CN)$_4$]$_2$ · 2H$_2$O} single crystal unit cell data
a (Å)	21.2083	21.2590
b (Å)	13.2861	12.9694
c (Å)	15.6911	15.4095
α (°)	90	90
β (°)	91.823	92.8110
γ (°)	90	90

Supplementary Figure 12: a) pXRD diffractogram of {Fe(**Br-pbpy**$^+$)$_2$[μ$_2$-Pt(CN)$_4$]$_2$·2H$_2$O} (GOF= 1.12, Rp= 2.10, wRp= 3.02) and (b) obtained unit cell parameters via refinement using corresponding single crystal data.

a)

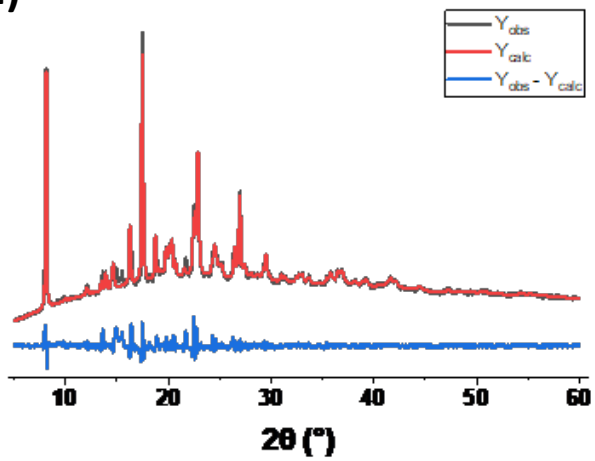

b)

	{Fe(**$COOCH_3$-pbpy$^+$**)$_2$[μ$_2$-Ni(CN)$_4$]$_2$ · 2H_2O} refined unit cell data (pXRD)	{Fe(**$COOCH_3$-pbpy$^+$**)$_2$[μ$_2$-Pt(CN)$_4$]$_2$ · 2H_2O} single crystal unit cell data
a (Å)	12.0809	12.0484
b (Å)	14.5458	14.6058
c (Å)	14.5214	14.0583
α (°)	90	90
β (°)	112.116	111.665
γ (°)	90	90

Supplementary Figure 13: a) pXRD diffractogram of {Fe(**$COOCH_3$-pbpy$^+$**)$_2$[μ$_2$-Ni(CN)$_4$]$_2$·xH_2O} (GOF= 2.15, Rp= 2.16, wRp= 3.51) and (b) obtained unit cell parameters via refinement using single crystal data of the Pt analogue.

a)

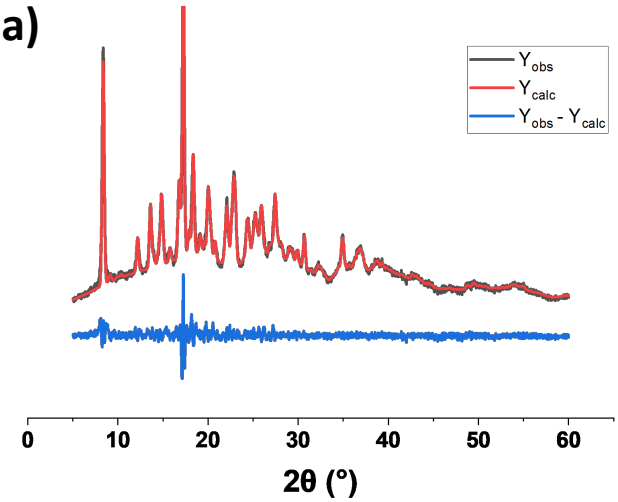

b)

	{Fe(**$COOCH_3$-pbpy$^+$**)$_2$[μ$_2$-Pt(CN)$_4$]$_2$ · 2H_2O} refined unit cell data (pXRD)	{Fe(**$COOCH_3$-pbpy$^+$**)$_2$[μ$_2$-Pt(CN)$_4$]$_2$ · 2H_2O} single crystal unit cell data
a (Å)	12.0317	12.0484
b (Å)	14.4969	14.6058
c (Å)	13.8660	14.0583
α (°)	90	90
β (°)	111.059	111.665
γ (°)	90	90

Supplementary Figure 14: a) pXRD diffractogram of {Fe(**$COOCH_3$-pbpy$^+$**)$_2$[μ$_2$-Pt(CN)$_4$]$_2$·xH_2O} (GOF= 1.37, Rp= 2.69, wRp= 3.89) and (b) obtained unit cell parameters via refinement using the corresponding single crystal data.

a)

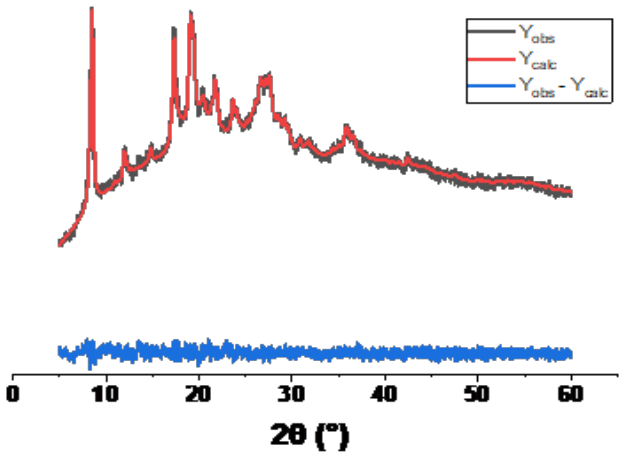

b)

	{Fe(**NO_2-pbpy$^+$**)$_2$[μ$_2$-Ni(CN)$_4$]$_2$ · 2H$_2$O} refined unit cell data (pXRD)	{Fe(**NO_2-pbpy$^+$**)$_2$[μ$_2$-Pd(CN)$_4$]$_2$ · 2H$_2$O} single crystal unit cell data
a (Å)	10.4004	10.4468
b (Å)	10.5467	10.5411
c (Å)	11.0064	10.7900
α (°)	81.229	82.13
β (°)	80.546	81.252
γ (°)	87.274	86.422

Supplementary Figure 15: a) pXRD diffractogram of {Fe(**NO_2-pbpy$^+$**)$_2$[μ$_2$-Ni(CN)$_4$]$_2$} (GOF= 0.89, Rp= 1.53, wRp= 1.98) and (b) obtained unit cell parameters via refinement using single crystal data of the Pd analogue.

a)

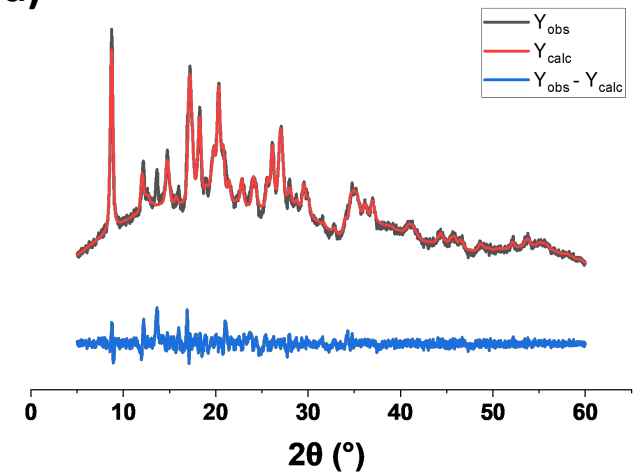

b)

	{Fe(**NO_2-pbpy$^+$**)$_2$[μ$_2$-Pt(CN)$_4$]$_2$ · 2H$_2$O} refined unit cell data (pXRD)	{Fe(**NO_2-pbpy$^+$**)$_2$[μ$_2$-Pd(CN)$_4$]$_2$ · 2H$_2$O} single crystal unit cell data
a (Å)	10.2337	10.4468
b (Å)	10.4269	10.5411
c (Å)	11.0970	10.7900
α (°)	83.018	82.13
β (°)	81.693	81.252
γ (°)	87.384	86.422

Supplementary Figure 16: a) pXRD diffractogram of {Fe(**NO_2-pbpy$^+$**)$_2$[μ$_2$-Pt(CN)$_4$]$_2$ · 2H$_2$O} (GOF= 1.36, Rp= 2.97, wRp= 4.09) and (b) obtained unit cell parameters via refinement using single crystal data of the Pd analogue.

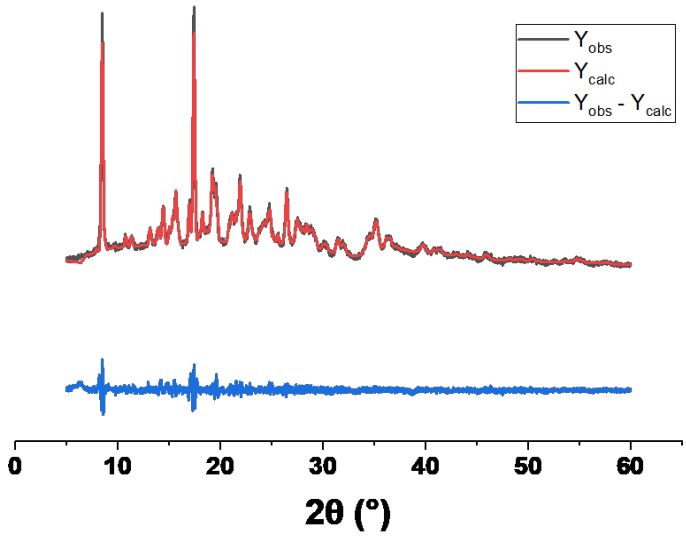

Supplementary Figure 17: pXRD diffractogram of **1b-Zn** {Zn(**CH_3-pbpy**$^+$)$_2$[μ_2-Pt(CN)$_4$]$_2$·2H_2O} (GOF= 1.13, Rp = 3.94, wRp = 5.49). The calculated diffraction pattern was refined using unit cell parameters of [Fe(CH_3-pbpy)$_2$[Pt(CN)$_4$]$_2$·2H_2O}. Obtained unit cell parameters: a= 20.9253, b= 13.2819, c= 15.6712, α= 90.000, β= 92.562, γ= 90.000.

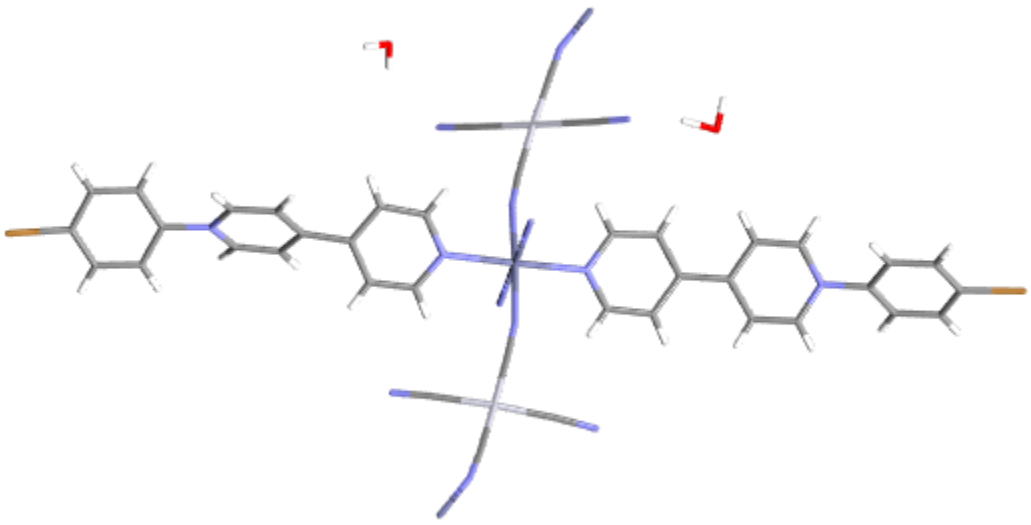

Supplementary Figure 18: Unit cell of **2b-Zn** {Zn(**Br-pbpy**$^+$)$_2$[μ_2-Pt(CN)$_4$]$_2$·2H_2O}, it is isostructural to the respective Fe^{II} compound (see also Supplementary Table 11).

2.4 Electronic spectroscopy

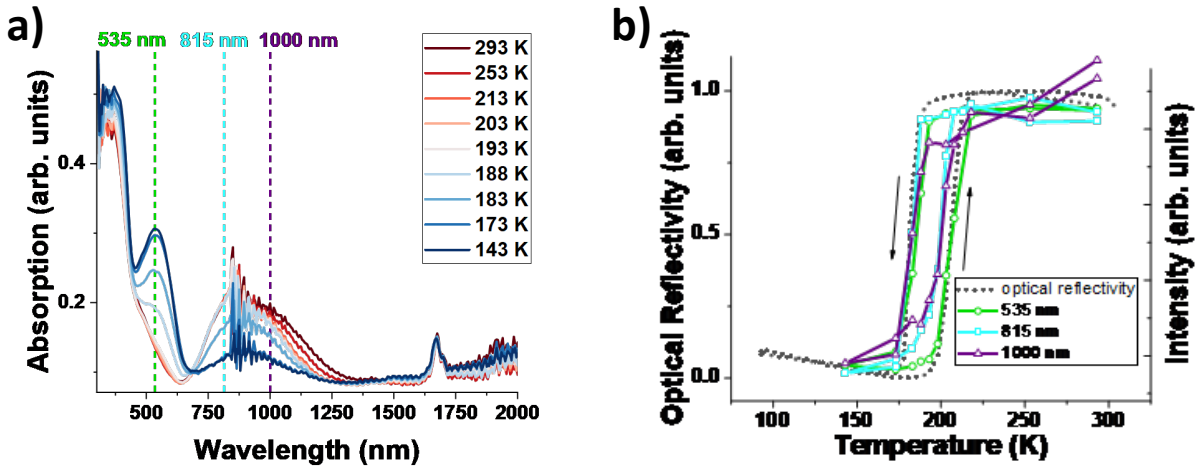

Supplementary Figure 19: a) Evolution of UV-vis-NIR absorption spectra of {Fe(**py**)$_2$[μ$_4$-Ni(CN)$_4$]·2H$_2$O} upon heating from 103 K, b) evolution of the absorption band intensities with temperature. The absorption band intensity scale for 535 nm (green) has been inverted to facilitate a comparison with the other absorption bands. Arrows indicate heating and cooling.

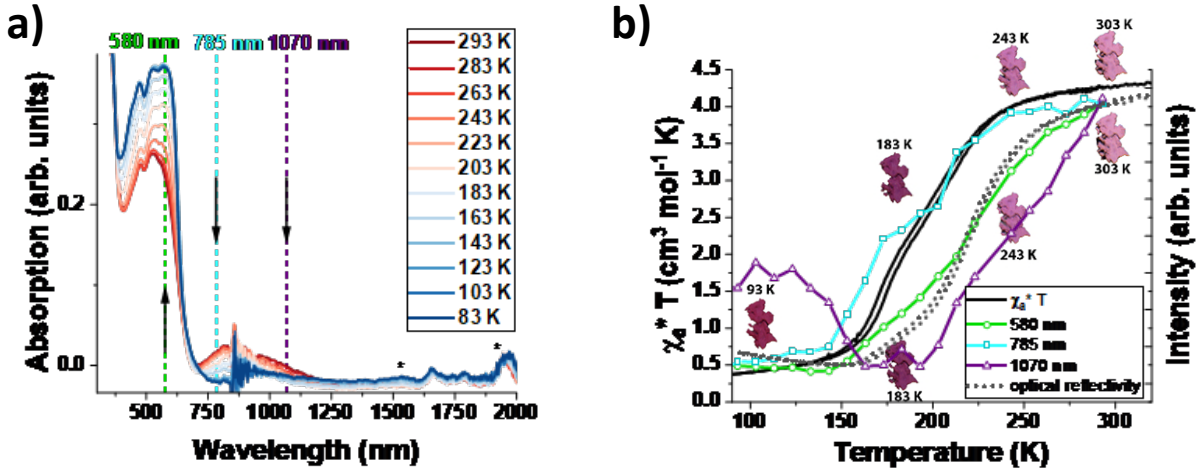

Supplementary Figure 20: a) Temperature dependent UV-vis-NIR absorption spectra of **1b** Fe(**CH$_3$-pbpy$^+$**)$_2$[μ$_2$-Ni(CN)$_4$]$_2$·2H$_2$O} upon cooling and b) comparison of the evolution of χ_aT of **1b** and the absorption intensities at selected wavelengths as a function of the temperature. The absorption intensity scale for 580 nm (green) has been inverted to facilitate a comparison with the optical behavior. The peaks marked with * stem from water/humidity.

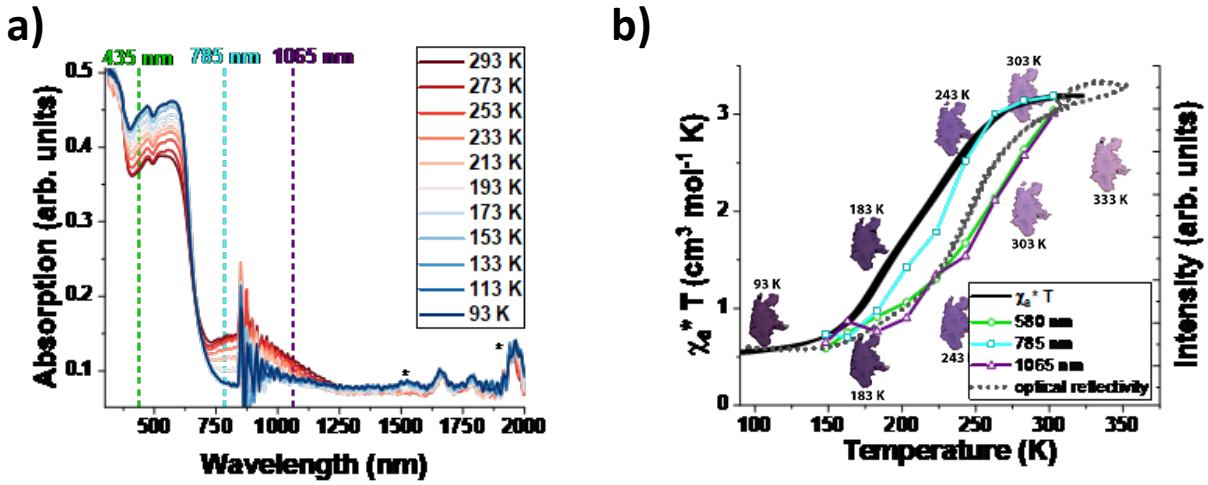

Supplementary Figure 21: a) Evolution of UV-vis-NIR absorption spectra of **2a** {Fe(**Br-pbpy**$^{+}$)$_2$[μ_2-Ni(CN)$_4$]$_2$·2H$_2$O} upon cooling, and b) comparison of the evolution of χ_aT of **2a** and the absorption intensities at selected wavelengths as a function of the temperature. The absorption intensity scale for 585 nm (green) has been inverted to facilitate a comparison with the optical behavior. The peaks marked with * stem from water/humidity.

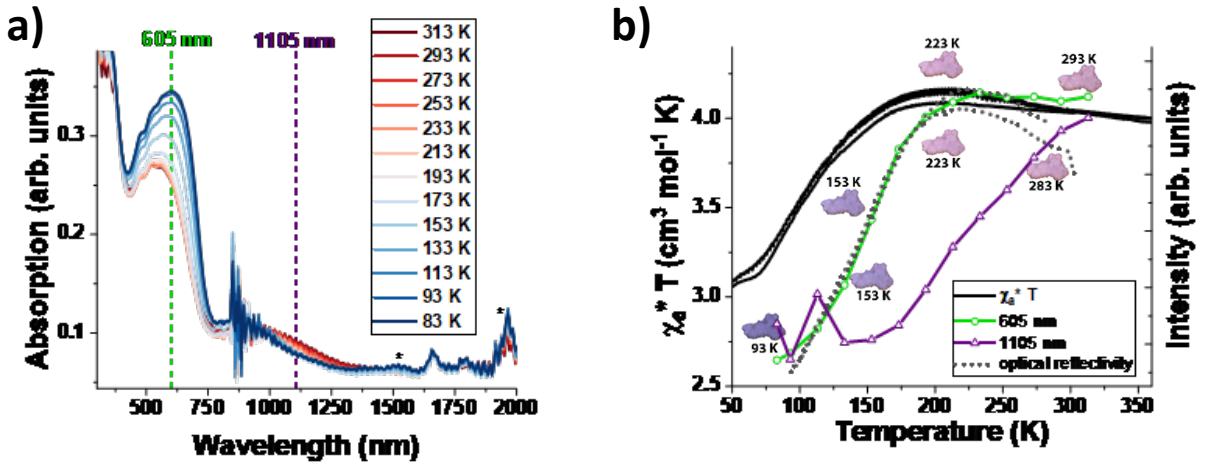

Supplementary Figure 22: a) Evolution of UV-vis-NIR absorption spectrum of **3a** {Fe(**CH$_3$OOC-pbpy**$^{+}$)$_2$[μ_2-Ni(CN)$_4$]$_2$·2H$_2$O} upon cooling, b) comparison of the evolution of χ_aT of **3a** and the absorption intensities at selected wavelengths as a function of the temperature. The absorption intensity scale for 605 nm (green) has been inverted to facilitate a comparison with the optical behavior. The peaks marked with * stem from water/humidity.

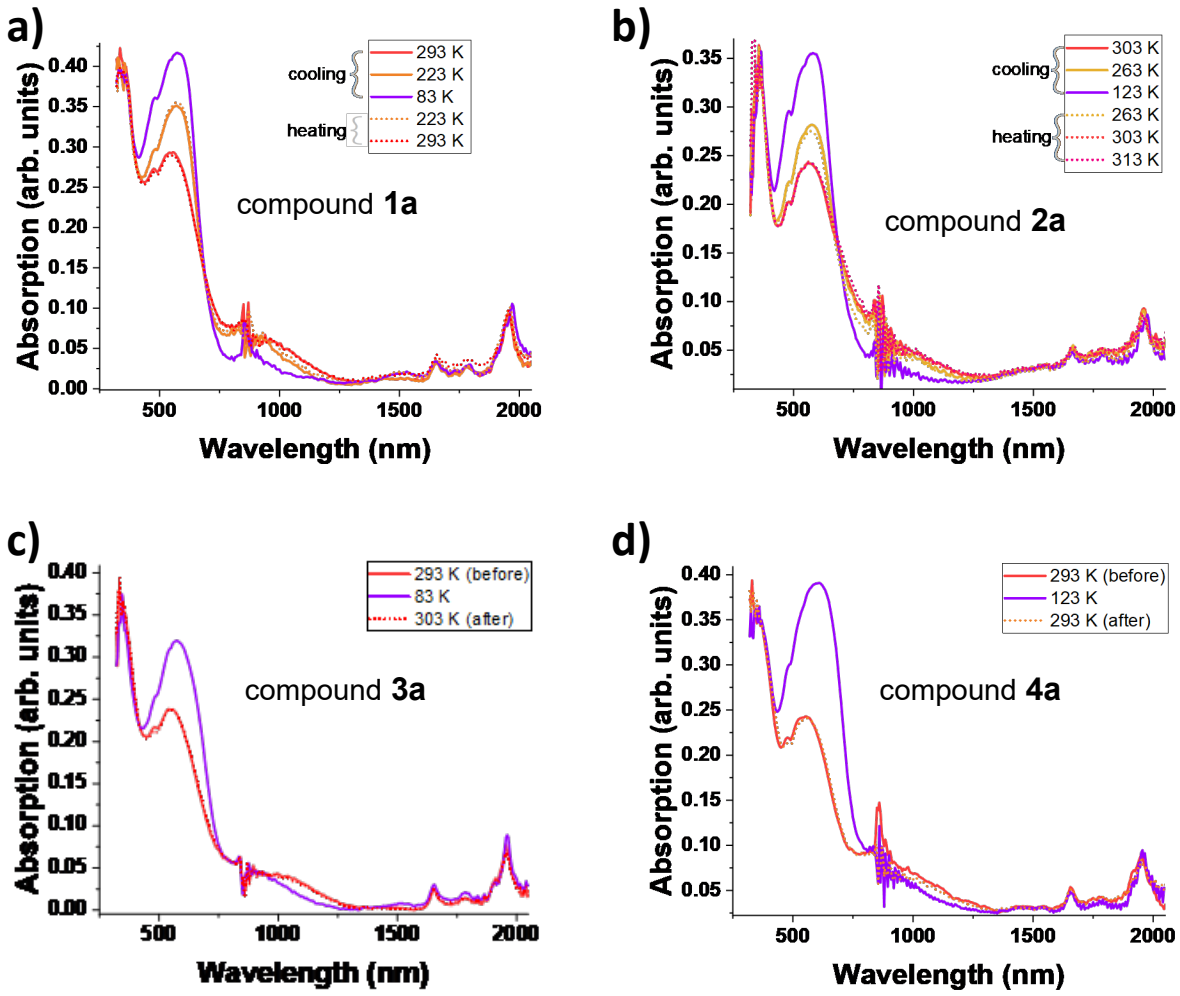

Supplementary Figure 23: Comparison of UV-Vis-NIR absorption spectra before and after cooling, showing that the observed thermochromism is fully reversible for all samples. a) Compound **1a**, b) compound **2a**, c) compound **3a** and d) compound **4a**.

2.5 Mössbauer spectroscopy

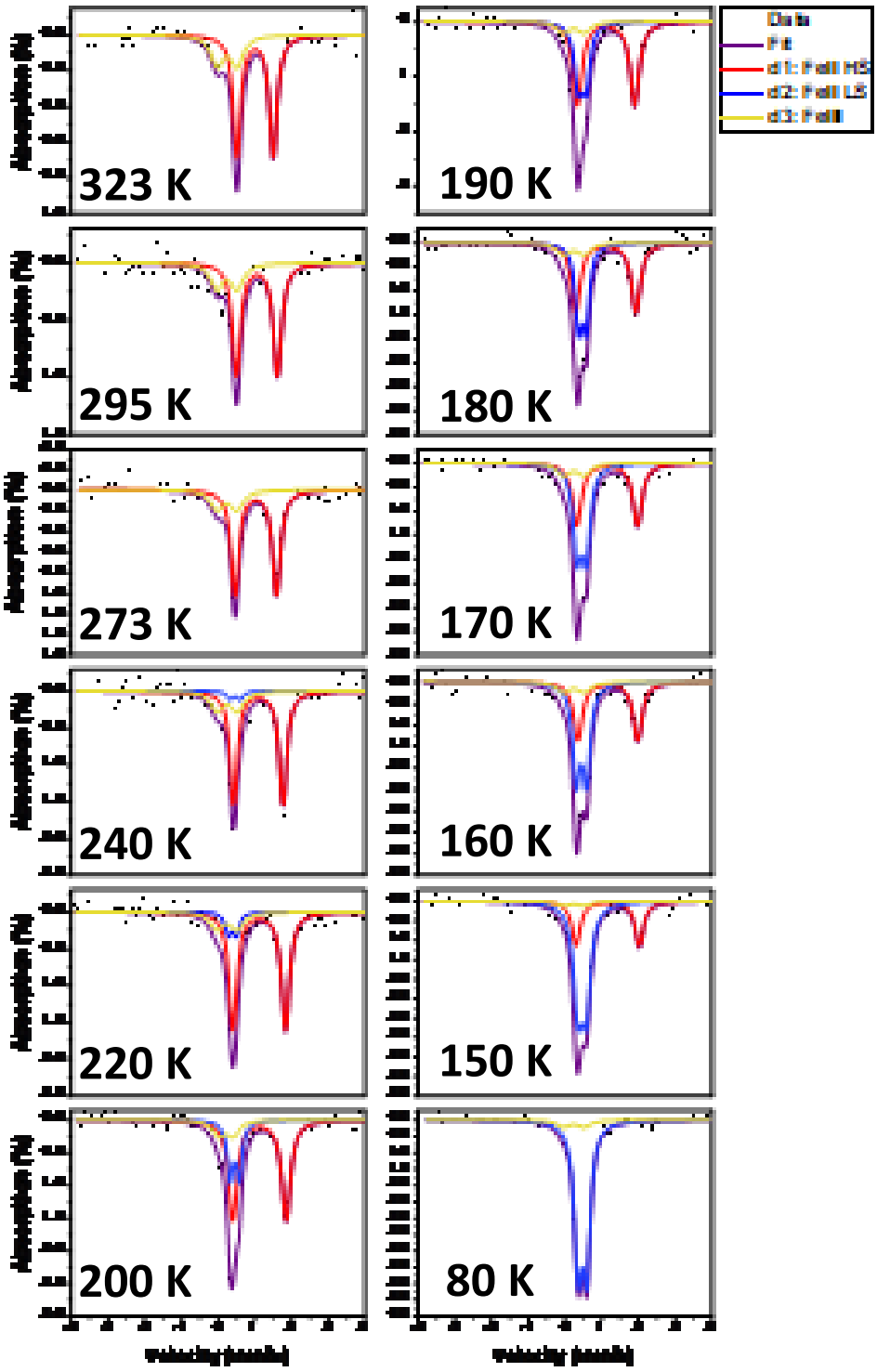

Supplementary Figure 24: ^{57}Fe Mössbauer spectra of {Fe(**CH$_3$-pbpy$^+$**)$_2$[μ_2-Ni(CN)$_4$]$_2$·2H$_2$O} at various temperatures.

Supplementary Table 1: Mössbauer parameters of doublets found in {Fe(**CH_3-pbpy$^+$**)$_2$[μ_2-Ni(CN)$_4$]$_2$·2H_2O}, see Supplementary Figure 24; parameters without error values were fixed for the fitting procedure.

Temperature (K)	**CS** (mm/s)		**QS** (mm/s)		**width** (mm/s)		**Population** (%)	
	Fe^{II} HS		Fe^{II} HS		Fe^{II} HS		Fe^{II} HS	
80	-	-	-	-	-	-	0	-
150	1.161	± 0.030	1.723	± 0.059	0.138	± 0.030	28.8	± 4.8
160	1.162	± 0.032	1.626	± 0.065	0.147	± 0.035	39.1	± 7.3
170	1.145	± 0.098	1.65	± 0.19	0.150	± 0.025	40.6	± 5.6
180	1.109	± 0.018	1.637	± 0.036	0.149	± 0.025	49.0	± 6.3
190	1.116	± 0.044	1.560	± 0.088	0.150	± 0.019	55.9	± 5.5
200	1.124	± 0.053	1.45	± 0.11	0.143	± 0.020	63.0	± 7.0
220	1.116	± 0.0086	1.432	± 0.017	0.132	± 0.016	72.6	± 6.6
273	1.0278	± 0.0084	1.132	± 0.017	0.130	± 0.013	77.5	± 6.5
295	1.056	± 0.013	1.113	± 0.026	0.134	± 0.019	74.4	± 9.1
323	1.005	± 0.017	0.987	± 0.035	0.127	± 0.016	71.3	± 6.9
	Fe^{II} LS		Fe^{II} LS		Fe^{II} LS		Fe^{II} LS	
80	0.4674	± 0.0040	0.2353	± 0.0064	0.1225	± 0.0067	92.3	± 4.0
150	0.461	± 0.014	0.231	± 0.024	0.141	± 0.016	66.9	± 5.7
160	0.445	± 0.018	0.277	± 0.039	0.122	± 0.020	51.7	± 7.7
170	0.451	± 0.067	0.25	± 0.13	0.132	± 0.018	48.9	-
180	0.466	± 0.015	0.210	± 0.023	0.108	± 0.017	39.6	-
190	0.460	± 0.057	0.21	± 0.10	0.127	± 0.024	34.2	-
200	0.440	± 0.027	0.255	± 0.042	0.098	± 0.031	24.2	± 4.7
220	0.386	± 0.048	0.222	± 0.096	0.103	± 0.051	10.4	-
273	-	-	-	-	-	-	0	-
295	-	-	-	-	-	-	0	-
323	-	-	-	-	-	-	0	-
	Fe^{III}		Fe^{III}		Fe^{III}		Fe^{III}	
80	0.24	-	0.56	-	0.21	-	7.7	± 4.4
150	0.24	-	0.56	-	0.21	-	4.3	± 5.5
160	0.24	-	0.56	-	0.21	-	9.3	± 7.8
170	0.24	-	0.56	-	0.21	-	10.5	± 4.1
180	0.24	-	0.56	-	0.21	-	11.3	± 4.4
190	0.24	-	0.56	-	0.21	-	10	± 4
200	0.24	-	0.56	-	0.21	-	12.8	-
220	0.24	-	0.56	-	0.21	-	17.0	± 4.7
273	0.24	-	0.56	-	0.21	-	22.5	± 5.2
295	0.24	-	0.56	-	0.21	-	25.6	± 7.2
323	0.241	± 0.100	0.55	± 0.17	0.206	± 0.080	28.7	± 7.5

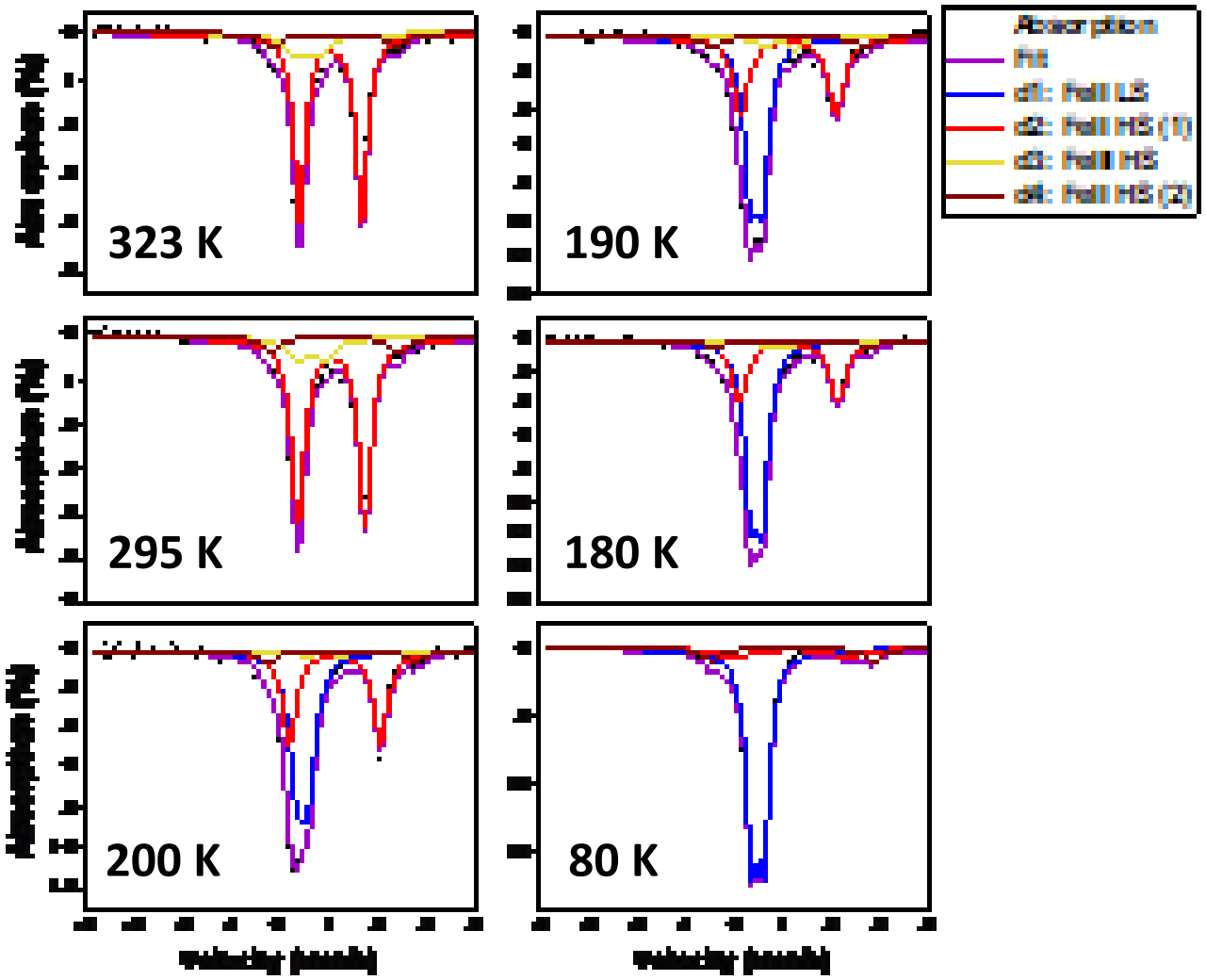

Supplementary Figure 25: ^{57}Fe Mössbauer spectra of {Fe(**Br-pbpy**$^{+}$)$_2$[μ_2-Ni(CN)$_4$]$_2$·2H$_2$O} at a selected temperatures. The sample is ^{57}Fe enriched.

Supplementary Table 2: Mössbauer parameters of doublets found in {^{57}Fe(**Br-pbpy^{+}**)$_2$[μ_2-Ni(CN)$_4$]$_2$·2H$_2$O}, see Supplementary Figure 25.

Temperature (K)	**CS** (mm/s)	**QS** (mm/s)	**width** (mm/s)	**Population** (%)
	Fe^{II} HS (1)	Fe^{II} HS (1)	Fe^{II} HS (1)	Fe^{II} HS (1)
80	1.156 ± 0.041	2.38 ± 0.13	0.322 ± 0.093	9.8 ± 3.5
180	1.1148 ± 0.0079	2.017 ± 0.016	0.197 ± 0.012	31.4 ± 1.7
190	1.1079 ± 0.0092	1.959 ± 0.018	0.194 ± 0.015	36.6 ± 2.5
200	1.118 ± 0.010	1.877 ± 0.020	0.175 ± 0.015	39.3 ± 2.8
295	1.0484 ± 0.0061	1.372 ± 0.012	0.1664 ± 0.0045	79.7 ± 2.0
323	1.0322 ± 0.0028	1.2699 ± 0.0055	0.1451 ± 0.0043	77.2 ± 2.0
	Fe^{II} LS	Fe^{II} LS	Fe^{II} LS	Fe^{II} LS
80	0.4820 ± 0.0015	0.2434 ± 0.0022	0.1441 ± 0.0021	82.43 ± 0.85
180	0.4536 ± 0.0050	0.2338 ± 0.0073	0.1558 ± 0.0070	60.7 ± 1.4
190	0.45 ± 0.20	0.24 ± 0.39	0.1578 ± 0.0082	54.0 ± 1.8
200	0.451 ± 0.056	0.23 ± 0.13	0.183 ± 0.022	52.4 ± 2.7
295	- -	- -	- -	0 -
323	- -	- -	- -	0 -
	Fe^{III}	Fe^{III}	Fe^{III}	Fe^{III}
80	- -	- -	- -	- -
180	0.880 ± 0.087	0.51 ± 0.17	0.16 -	3.3 ± 1.1
190	0.9 ± 2.5	0.6 ± 5.0	0.16 -	4.3 ± 1.6
200	0.9 ± 1.0	0.7 ± 2.1	0.16 -	2.4 ± 1.9
295	0.633 ± 0.079	0.57 ± 0.14	0.25 -	12.7 ± 1.5
323	0.541 ± 0.040	0.495 ± 0.074	0.25 -	14.7 ± 1.6
	Fe^{II} HS (2)	Fe^{II} HS (2)	Fe^{II} HS (2)	Fe^{II} HS (2)
80	1.181 ± 0.021	3.323 ± 0.058	0.197 ± 0.050	7.7 ± 2.6
180	1.164 ± 0.045	3.196 ± 0.095	0.2 -	4.6 ± 1.0
190	1.111 ± 0.059	3.14 ± 0.12	0.2 -	5.1 ± 1.4
200	1.241 ± 0.093	3.01 ± 0.20	0.2 -	8.1 ± 2.4
295	1.125 ± 0.039	2.615 ± 0.080	0.2 -	7.5 ± 1.3
323	1.104 ± 0.039	2.529 ± 0.079	0.2 -	8.1 ± 1.3

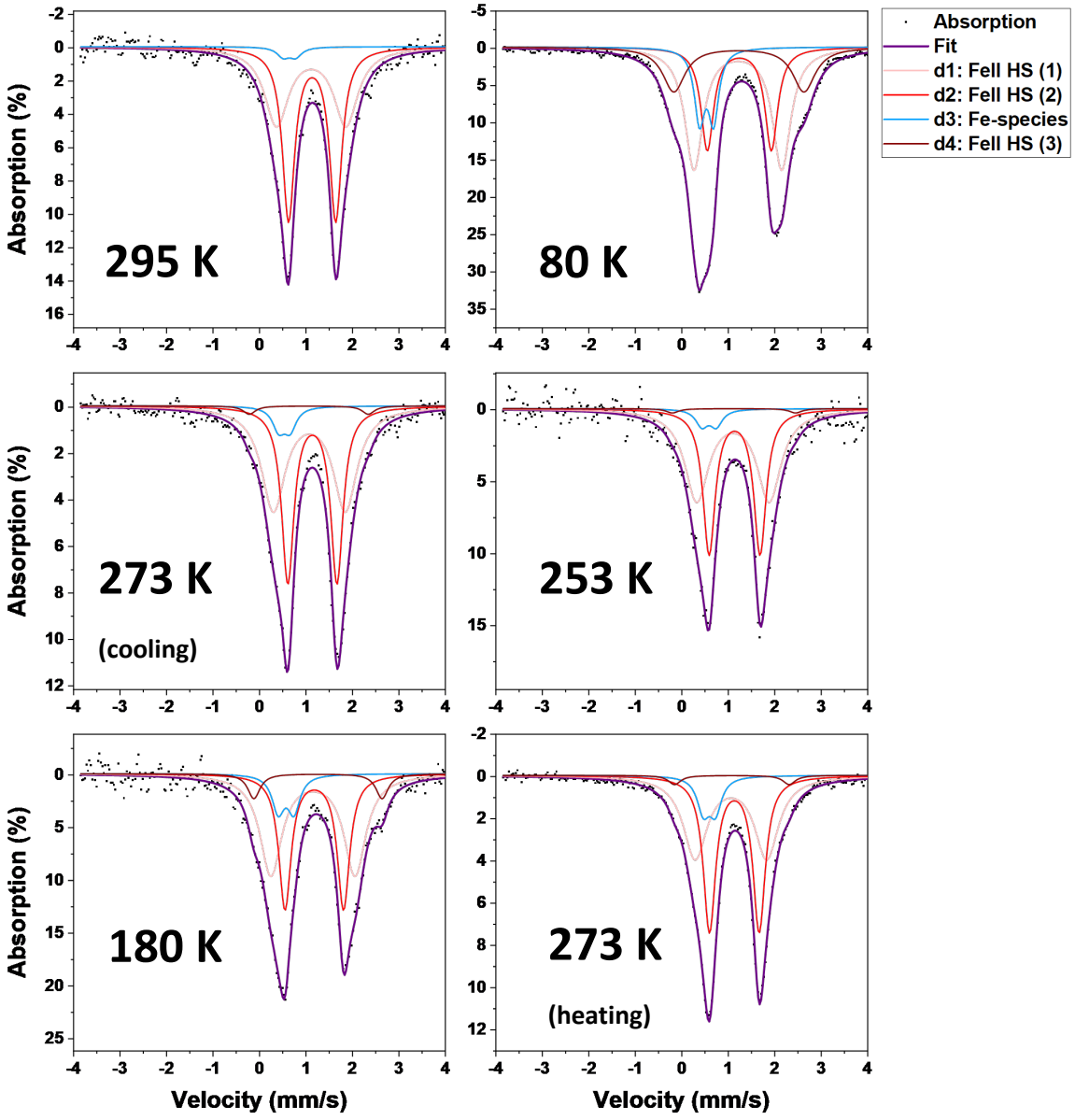

Supplementary Figure 26: ^{57}Fe Mössbauer spectra of {Fe(**NO$_2$-pbpy$^+$**)$_2$[μ$_2$-Ni(CN)$_4$]$_2$} at selected temperatures, the sample is ^{57}Fe enriched. Due to the hysteresis loop observed in optical measurements, the spectra at 253 K and 273 K (heating) where collected after the sample was cooled to 80 K.

Supplementary Table 3: Mössbauer parameters of doublets found in {^{57}Fe(**NO$_2$-pbpy$^+$**)$_2$[μ_2-Ni(CN)$_4$]$_2$}, see Supplementary Figure 26.

Temperature (K)	**CS** (mm/s)		**QS** (mm/s)		**width** (mm/s)		**Population** (%)	
	Fe^{II} HS (1)		Fe^{II} HS (1)		Fe^{II} HS (1)		Fe^{II} HS (1)	
295	1.114	± 0.020	1.493	± 0.085	0.31	-	45.2	± 7.4
273	1.074	± 0.007	1.547	± 0.015	0.31	-	49.1	± 5.5
180	1.15	± 0.021	1.81	± 0.18	0.284	± 0.044	47.6	± 9.5
80	1.2068	± 0.0034	1.888	± 0.030	0.293	± 0.024	42.1	± 7.5
253	1.101	± 0.031	1.56	± 0.23	0.31	-	52	± 13
273	1.058	± 0.0081	1.539	± 0.044	0.31	-	44.4	± 3.6
	Fe^{II} HS (2)		Fe^{II} HS (2)		Fe^{II} HS (2)		Fe^{II} HS (2)	
295	1.1330	± 0.0055	1.016	± 0.013	0.16	-	51.9	± 6.1
273	1.1380	± 0.0097	1.057	± 0.022	0.16	-	49.4	± 4.4
180	1.1785	± 0.0081	1.260	± 0.024	0.16	-	35.0	± 5.9
80	1.2385	± 0.0031	1.378	± 0.022	0.165	± 0.016	24.9	± 5.5
253	1.136	± 0.010	1.095	± 0.027	0.16	-	34	± 10
273	1.1305	± 0.0031	1.0689	± 0.0066	0.16	-	52.9	± 3.0
	Fe-species		Fe-species		Fe-species		Fe-species	
295	0.64	± 0.13	0.27	± 0.29	0.16	-	2.9	± 1.6
273	0.536	± 0.065	0.24	± 0.18	0.16	-	5.6	± 1.1
180	0.572	± 0.045	0.338	± 0.089	0.16	-	9.7	± 1.8
80	0.5326	± 0.0076	0.302	± 0.011	0.1335	± 0.0059	13.85	± 0.39
253	0.59	± 0.12	0.31	± 0.29	0.16	-	4.9	± 2.6
273	0.594	± 0.018	0.258	± 0.045	0.16	-	9.60	± 0.68
	Fe^{II} HS (3)		Fe^{II} HS (3)		Fe^{II} HS (3)		Fe^{II} HS (3)	
295	-	-	-	-	-	-	-	-
273	1.061	± 0.095	2.56	± 0.20	0.16	-	2.1	± 1.1
180	1.259	± 0.047	2.758	± 0.097	0.16	-	6.7	± 2.3
80	1.2290	± 0.0088	2.800	± 0.037	0.293	± 0.024	19.2	± 2.7
253	1.12	± 0.35	2.65	± 0.73	0.16	-	1.3	± 2.5
273	1.078	± 0.045	2.466	± 0.096	0.16	-	2.59	± 0.72

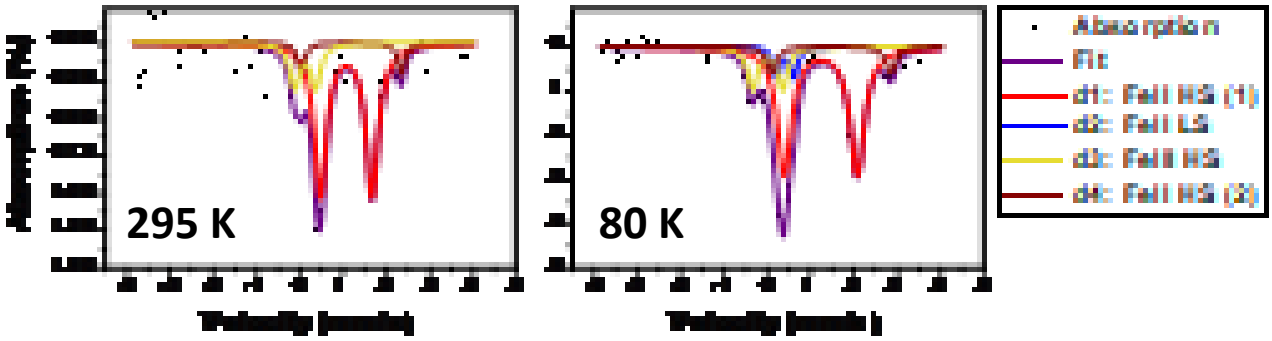

Supplementary Figure 27: ^{57}Fe Mössbauer spectra of {Fe(**COOCH$_3$-pbpy$^+$**)$_2$[μ$_2$-Ni(CN)$_4$]$_2$} at 295 K and 80 K.

Supplementary Table 4: Mössbauer parameters of doublets found in {Fe(**COOCH$_3$-pbpy$^+$**)$_2$[μ$_2$-Ni(CN)$_4$]$_2$}, see Supplementary Figure 27.

Temperature (K)	**CS** (mm/s)	**QS** (mm/s)	**width** (mm/s)	**Population** (%)
	Fe^{II} HS (1)	Fe^{II} HS (1)	Fe^{II} HS (1)	Fe^{II} HS (1)
80	1.238	± 0.022	1.692	± 0.045
295	1.076	± 0.023	1.203	± 0.046
	Fe^{II} LS	Fe^{II} LS	Fe^{II} LS	Fe^{II} LS
80	0.420 ± 0.039	0.397 ± 0.072	0.101 ± 0.056	7.8 ± 4.0
295	- -	- -	- -	- -
	Fe^{III}	Fe^{III}	Fe^{III}	Fe^{III}
80	0.000 ± 0.058	0.70 ± 0.11	0.141 ± 0.051	15.5 ± 4.6
295	0.120 ± 0.072	0.49 ± 0.13	0.14 ± 0.10	17.1 ± 7.9
	Fe^{II} HS (2)	Fe^{II} HS (2)	Fe^{II} HS (2)	Fe^{II} HS (2)
80	1.472 ± 0.049	2.752 ± 0.097	0.140 ± 0.077	9.5 ± 4.4
295	1.178 ± 0.074	2.300 ± 0.015	0.10 ± 0.11	8.6 ± 8.4

2.6 Raman spectroscopy

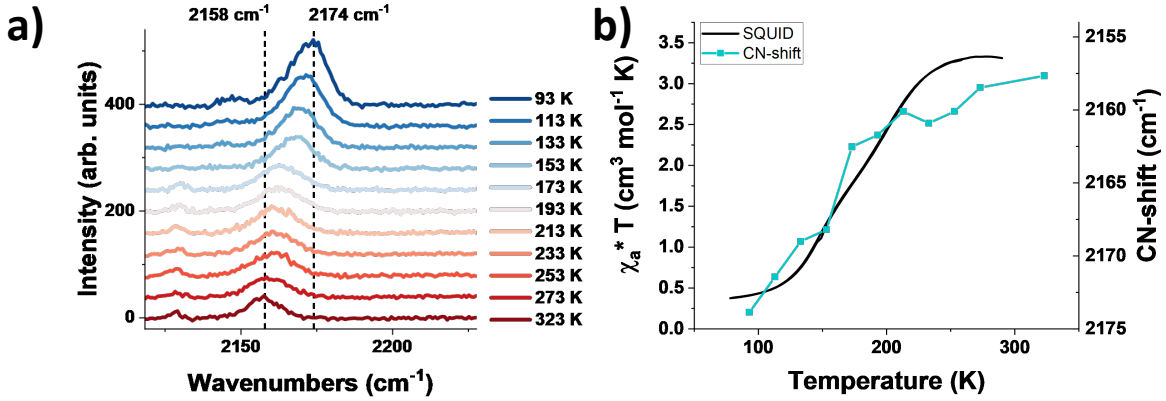

Supplementary Figure 28: a) Shift of the CN modes in temperature dependent Raman measurements of **1a** {Fe(**CH_3-pbpy$^+$**)$_2$[μ$_2$-Ni(CN)$_4$]$_2$·2H$_2$O}. b) Comparison of the magnetic susceptibility to the shift of the CN modes in temperature for **1a**.

2.7 Infrared spectroscopy

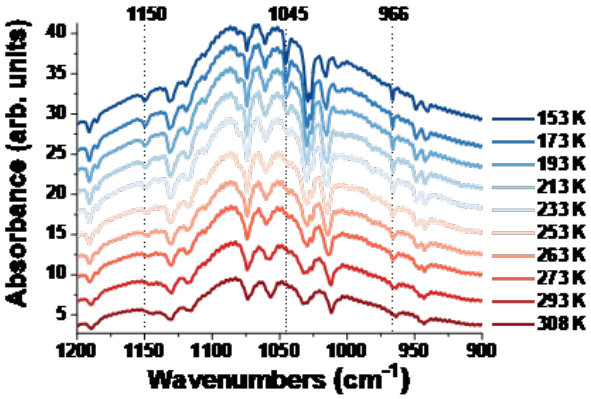

Supplementary Figure 29: Temperature dependent IR absorption spectra of **1a** {Fe(**CH_3-pbpy$^+$**)$_2$[μ$_2$-Ni(CN)$_4$]$_2$·2H$_2$O}.

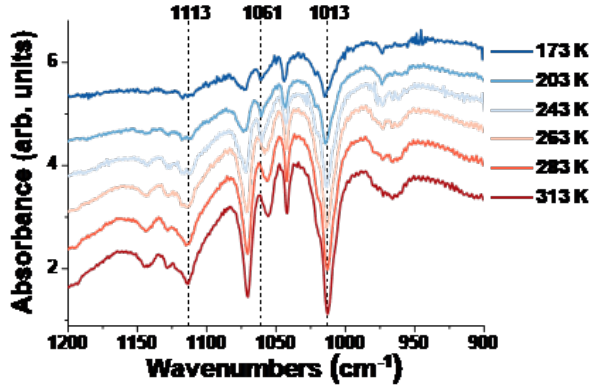

Supplementary Figure 30: Temperature dependent IR absorption spectra of **4a** {Fe(**NO_2-pbpy$^+$**)$_2$[μ$_2$-Ni(CN)$_4$]$_2$·2H$_2$O}.

3 Supplementary Discussion

3.1 DFT

All calculations have been performed with the ADF program [1] using the statistical average of orbital potentials (SAOP) exchange-correlation potential and including scalar-relativistic effects within the zero-order regular approximation (ZORA) [2]. The atoms were described by relativistic all-electron Slater-type basis sets from the ADF program [3]: the TZP basis set of triple-ζ polarized quality was employed for the Fe and Pt atoms, and the DZP basis set of double-ζ polarized quality for the N, C and H atoms. The fragments were solvated in water using the conductor-like screening model of solvation (COSMO) [4]. The electronic absorption properties have been studied by performing electronic excitation calculations within linear response in time-dependent density functional theory (LR-TDDFT) [5] and the Tamm-Dancoff (TDA) approximation [6]. The analysis of the predicted transitions were done in terms of transition between occupied and virtual natural transition orbitals (NTO) [7]. The calculations were run restricted for the LS state and unrestricted for the considered HS state with the projection of the total spin moment S along the z axis constrained to MS = +S.

The {Fe(**CH_3-pbpy$^+$**)$_2$[μ_2-Pt(CN)$_4$]$_2$·2H_2O} compound, has been modelled using a molecular fragment consisting of the Fe(II) ion, the two **CH_3-pbpy$^+$** ligands and the four neighbouring [Pt(CN)$_4$]- moieties: namely, the {Fe(**CH_3-pbpy$^+$**)$_2$[μ_2-Pt(CN)$_4$]$_4$}$^{4-}$ complex. The complex has been studied in the LS state (total electronic spin S = 0) and in the HS state (S = 2). The adopted HS and LS geometries correspond to those found for this fragment in the crystal structures at 300 K and 150 K, respectively.

In order to get insight into the electronic absorption properties of the compound, linear response in time-dependent density functional theory (LR-TDDFT) has been applied to the characterization of the spectra of the LS and HS {Fe(**CH_3-pbpy$^+$**)$_2$[μ_2-Pt(CN)$_4$]$_4$}$^{4-}$ complexes.

The influence of an electron transfer on the optical properties in the HS state has also been probed first by adding one electron to the system in the HS state, its spin being ferromagnetically coupled to the one of the magnetic center; that is, S = 5/2 in the HS state. The plot of the spin density obtained by the SCF calculations shows that the additional electron goes to one of the **CH_3-pbpy$^+$** ligands yielding the {Fe(**CH_3-pbpy$^+$**)(**CH_3-pbpy$^{\bullet}$**)[μ_2-Pt(CN)$_4$]$_4$}$^{5-}$ complex. Unfortunately, the examination of the frontier molecular orbitals (MOs) shows that the α-HOMO localized on the reduced **CH_3-pbpy$^{\bullet}$** ligand is quasi-degenerate with the α-LUMO of similar shape localized on the ligand. Therefore, the characterized electronic state is nearly degenerate with the one associated with the electron on the other **CH_3-pbpy$^+$** ligand. This near degeneracy invalidates the use of LR-TDDFT calculations and calls for the use of computationally more demanding multireference wavefunction-based methods. This observed equivalence of the **CH_3-pbpy$^+$** ligands is probably due to the fact that the adopted model does not fully account for the influence of the crystal packing and might hence be lifted by resorting to an extended model system, which includes neighbouring CN^- or **CH_3-pbpy$^+$** moieties, or which includes optimized point charges that help mimic the influence of the crystalline environment. The use of a multireference wavefunction-based method is beyond the scope of the present study, as is the use of a larger model. The more so as significant insight into the influence of an electron transfer on the optical properties could be gained by performing LR-TDDFT calculations on the doubly reduced HS fragment (S = 3) {Fe(**CH_3-pbpy$^{\bullet}$**)$_2$[μ_2-Pt(CN)$_4$]$_4$}$^{6-}$. Table 1 shows the total electronic spin, the number of unpaired electrons on the Fe atom, and the isodensity plot as found for the considered HS fragments. For all fragments, there are about 4 unpaired electrons on the Fe atom, which is consistent with a HS Fe(II) center. Upon addition of one or two electrons, one or both **CH_3-pbpy$^+$** ligands are reduced respectively, as evidenced by the spin density found on the ligands.

Supplementary Table 5: Characterized HS fragments: total electronic spin S; number n_α(Fe) of unpaired (α) electrons on the Fe atom as obtained from the post-SCF population analysis; plot of the spin density (SAOP results).

	S	n_α(Fe)	spin density
HS {Fe(**CH_3-pbpy$^+$**)$_2$[μ$_2$-Pt(CN)$_4$]$_4$}$^{4-}$	2	3.9*e*	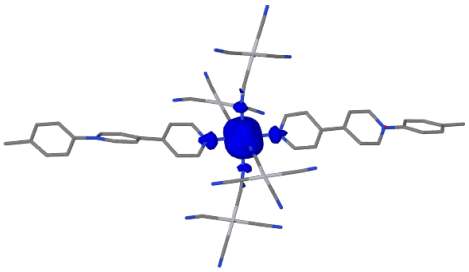
HS {Fe(**CH_3-pbpy$^+$**)(**CH_3-pbpy$^\bullet$**)[μ$_2$-Pt(CN)$_4$]$_4$}$^{5-}$	5/2	3.8*e*	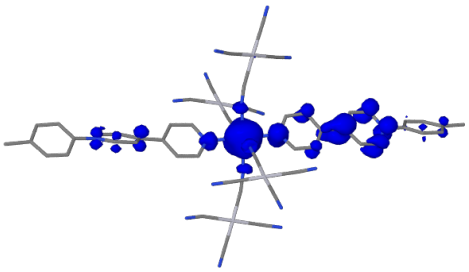
HS {Fe(**CH_3-pbpy$^\bullet$**)$_2$[μ$_2$-Pt(CN)$_4$]$_4$}$^{6-}$	3	3.8*e*	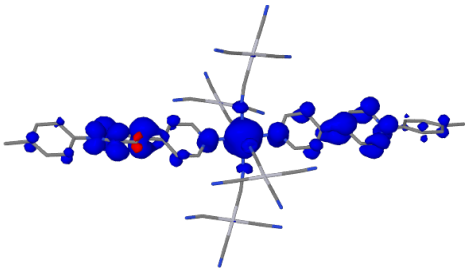

For the LS and HS fragments of {Fe(**CH_3-pbpy$^+$**)$_2$[μ$_2$-Pt(CN)$_4$]$_4$}$^{4-}$ as well as the HS fragment {Fe(**CH_3-pbpy$^\bullet$**)$_2$[μ$_2$-Pt(CN)$_4$]$_4$}$^{6-}$, the energy and oscillator strength of 80 lowest-lying transitions were determined by the LR-TD-DFT calculations. Figure 8 in main text shows the LS and HS spectra obtained by convoluting the oscillator strengths with Gaussians having a full-width at half-maximum (FWHM) of 2000 cm^{-1}.

The low-energy parts of the calculated spectra of LS {Fe(**CH_3-pbpy$^+$**)$_2$[μ$_2$-Pt(CN)$_4$]$_4$}$^{4-}$ and HS {Fe(**CH_3-pbpy$^+$**)$_2$[μ$_2$-Pt(CN)$_4$]$_4$}$^{4-}$ spectra are dominated by an intense Fe → **CH_3-pbpy$^+$** MLCT transition located at 763 nm and 1185 nm, respectively (see Tables S2 and S3 which summarize the LR-TDDFT results for the 20 lowest-lying transitions in LS and in HS {Fe(**CH_3-pbpy$^+$**)$_2$[μ$_2$-Pt(CN)$_4$]$_4$}^{4}, respectively). For LS (respectively, HS) {Fe(**CH_3-pbpy$^+$**)$_2$[μ$_2$-Pt(CN)$_4$]$_4$}$^{4-}$, this MLCT band corresponds to the experimental band whose intensity is observed at 580 nm (respectively, 1065 nm) and increases (respectively, decreases) with increasing temperature (compare Fig. 3(a)). The red-shift of the calculated spectra can be ascribed to the approximations underlying the LR-TD-DFT calculations and possibly to the use of a molecular fragment and hence to the neglect of the crystalline environment.

The features of the 30 lowest-lying transitions determined for the doubly reduced HS fragment {Fe(**CH_3-pbpy$^\bullet$**)$_2$[μ$_2$-Pt(CN)$_4$]$_4$}$^{6-}$ are summarized in SI Supplementary Table 4. Its inspection shows that the two intense bands observed in the calculated spectrum of the reduced species (Fig. 4, yellow) are independent π → π transitions occurring at 796 nm and 663 nm and centered each on one or the other reduced ligand. The overlap of these intra-ligand absorption bands with the MLCT

bands found in the calculated spectra of LS and HS {Fe(**CH_3-pbpy$^+$**)$_2$[μ_2-Pt(CN)$_4$]$_4$}$^{4-}$ supports the conclusion drawn from the experiments that the temperature dependence of the absorption intensity at 785 nm is likely due to the presence of reduced **CH_3-pbpy$^\bullet$** ligands at elevated temperatures.

Supplementary Table 6: Characterization of the 20 lowest-lying transitions in the LS {Fe(**CH_3-pbpy$^+$**)$_2$[μ_2-Pt(CN)$_4$]$_4$}$^{4-}$ fragment with the transition energy (E), wavelength λ, oscillator strength (f), and the excited state; description in terms of transitions between occupied and virtual NTOs (SAOP results).

E / cm^{-1}	λ / nm	f	State	NTO→NTO transitions		
				%	occupied	→ virtual
12511	799	0.0001	1^{1}A	100	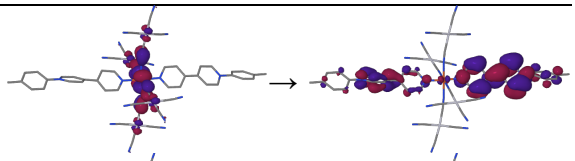	
12781	782	0.0135	2^{1}A	100	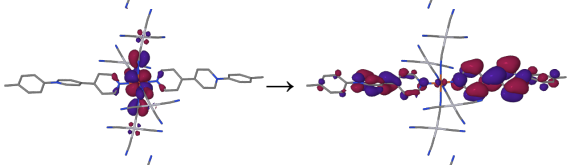	
13102	763	0.4059	3^{1}A	99	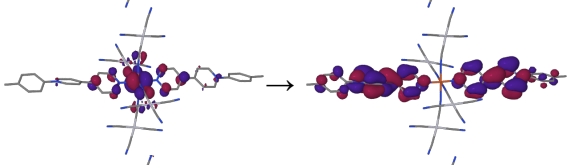	
13418	745	0.0000	4^{1}A	100	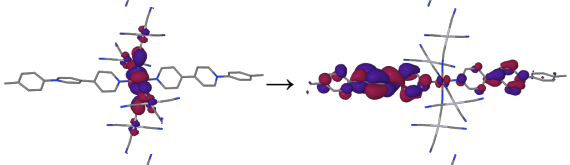	
13729	728	0.0010	5^{1}A	100	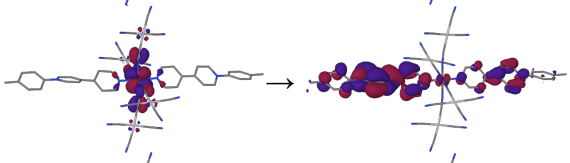	
15269	655	0.0165	6^{1}A	97	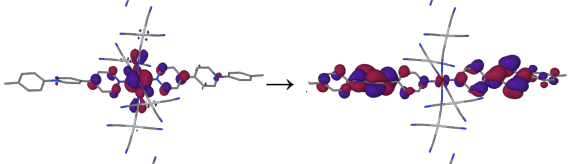	
21626	462	0.0037	7^{1}A	100	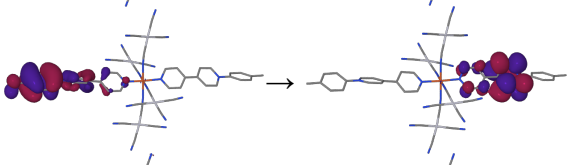	
22952	436	0.0000	8^{1}A	100	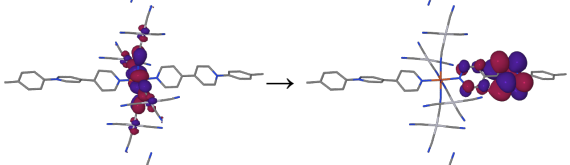	
23133	432	0.0028	9^{1}A	93	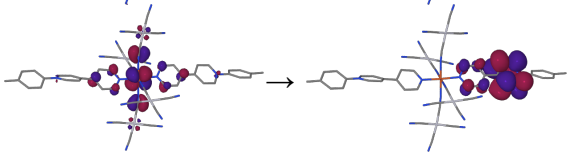	

23138	432	0.0337	10^1A	93	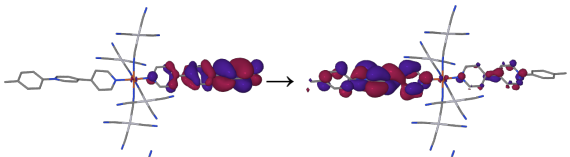
23246	430	0.0006	11^1A	100	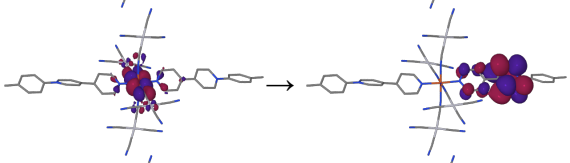
23520	425	0.0002	12^1A	100	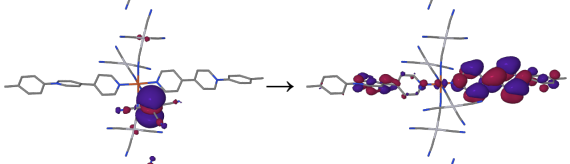
23598	424	0.0001	13^1A	100	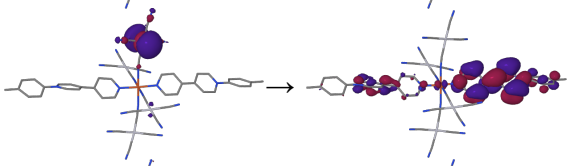
23787	420	0.0000	14^1A	100	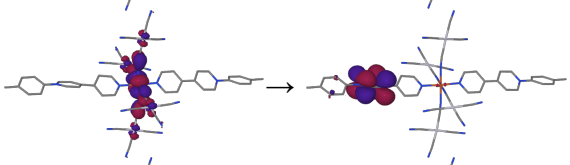
23916	418	0.0001	15^1A	100	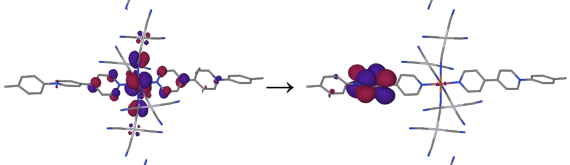
24017	416	0.5642	16^1A	97	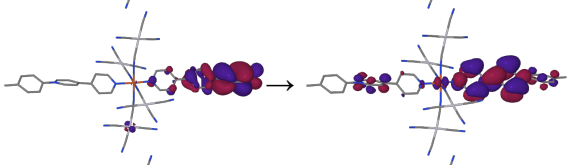
24064	416	0.0000	17^1A	99	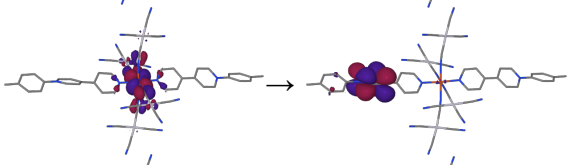
24068	415	0.0064	18^1A	99	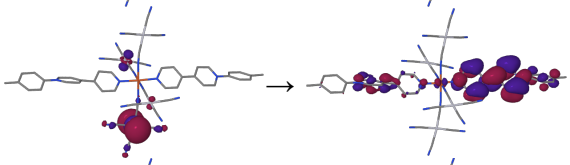
24108	415	0.0019	19^1A	100	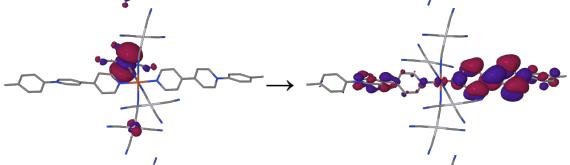
24255	412	0.4711	20^1A	96	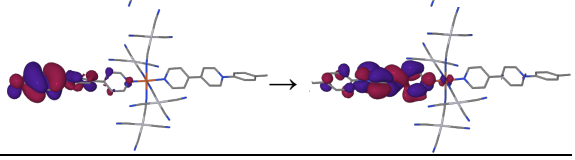

Supplementary Table 7: Characterization of the 20 lowest-lying transitions in the HS {Fe(**CH_3-pbpy$^+$**)$_2$[μ_2-Pt(CN)$_4$]$_4$} fragment with the transition energy (E), wavelength λ, oscillator strength (f), and the excited state; description in terms of transitions between occupied and virtual NTOs (SAOP results).

E / cm^{-1}	λ / nm	f	State	NTO→NTO transitions			
				%	Spin	occupied	→ virtual
8439	1185	0.2237	1^5A	100	β	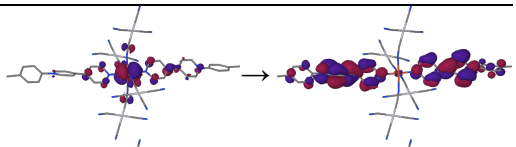	
10926	915	0.0197	2^5A	97	β	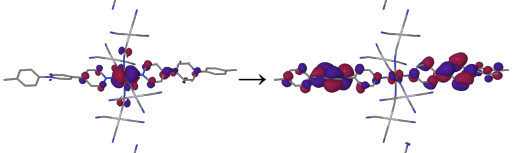	
12959	772	0.0002	3^5A	100	β	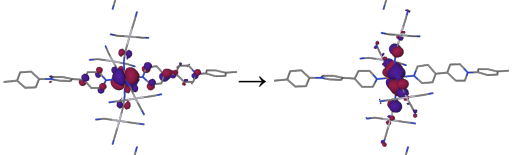	
13253	755	0.0001	4^5A	100	β	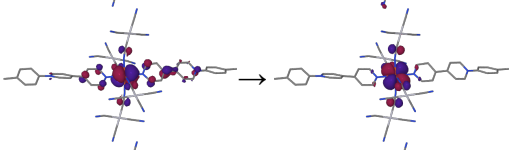	
15842	631	0.0023	5^5A	100	α	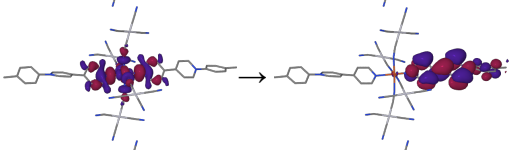	
18005	555	0.0004	6^5A	100	α	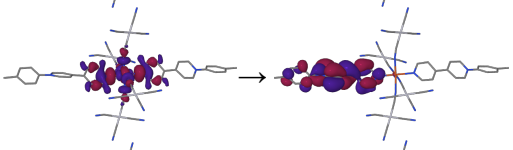	
18835	531	0.0370	7^5A	69	α	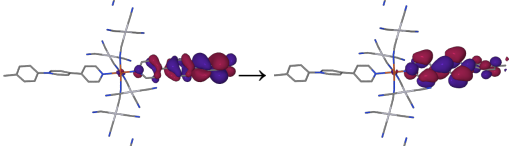	
				31	β	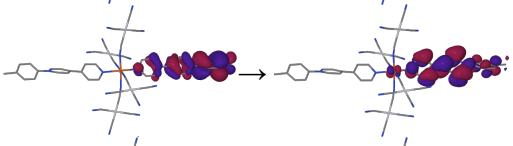	
20259	494	0.0003	8^5A	99	α	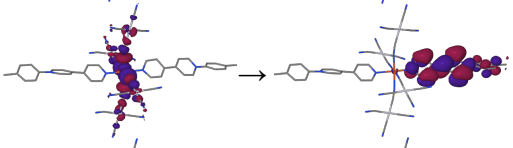	
20502	488	0.0180	9^5A	99	β	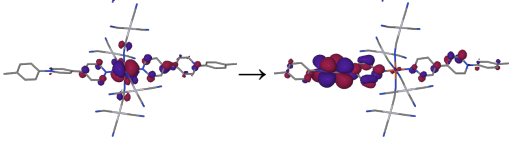	

20884	479	0.0080	10^5A	60	α	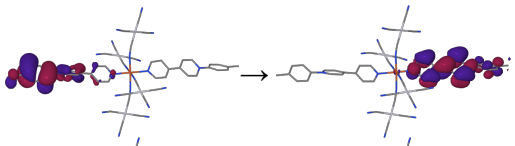
				40	β	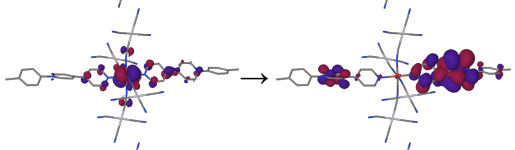
20888	479	0.0177	11^5A	58	β	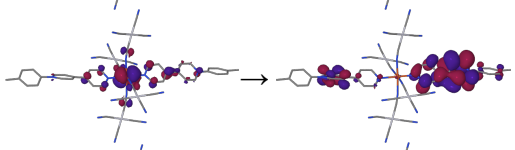
				41	α	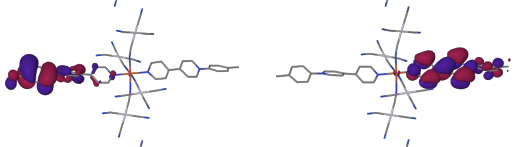
21234	471	0.0008	12^5A	99	β	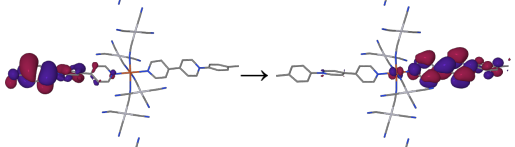
21399	467	0.1055	13^5A	85	β	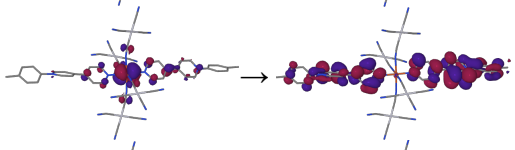
				10	β	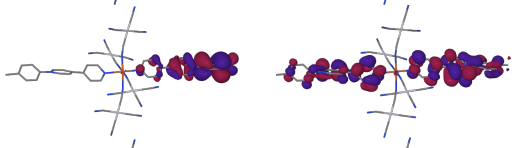
21638	462	0.0005	14^5A	100	α	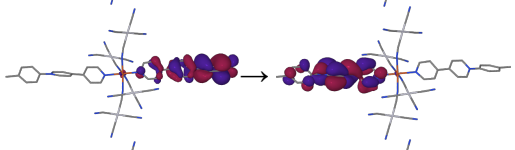
21915	456	0.0257	15^5A	88	β	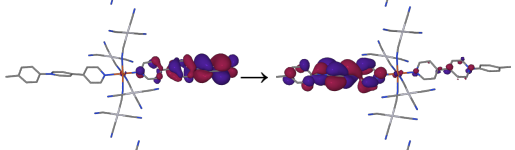
22172	451	0.0831	16^5A	58	β	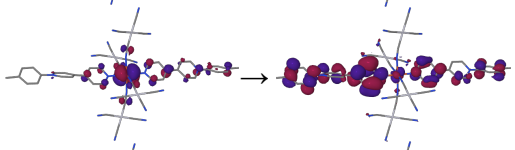
				30	β	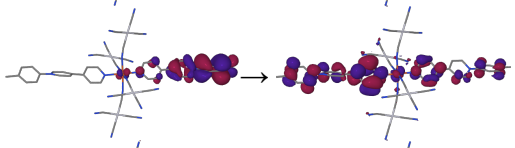
22377	447	0.0038	17^5A	69	α	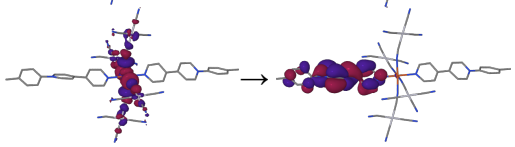

				30	β	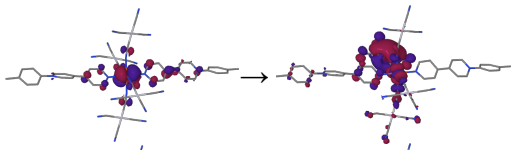
22464	445	0.0073	18^5A	67	α	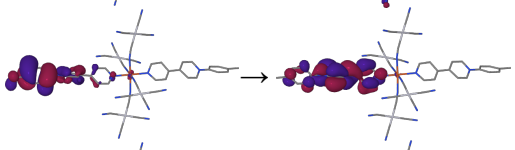
				32	β	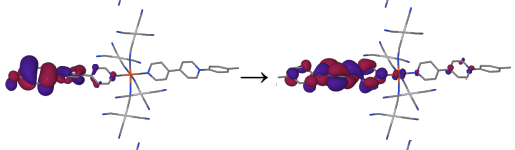
22563	443	0.0065	19^5A	70	β	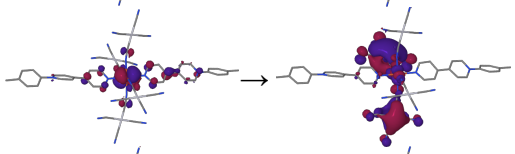
				27	α	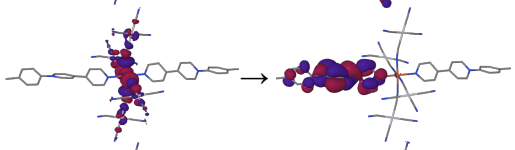
22791	439	0.2058	20^5A	53	β	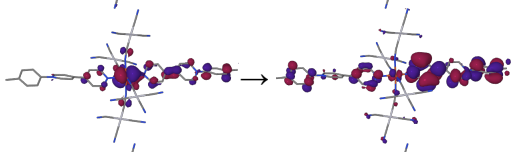
				31	β	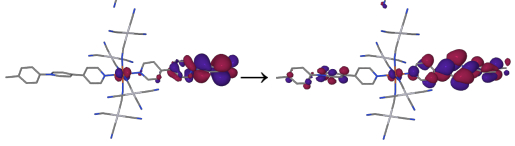
				12	α	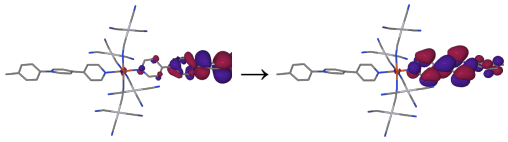

Supplementary Table 8: Characterization of the 30 lowest-lying transitions in the HS {Fe(**CH_3-pbpy$^{\bullet}$**)$_2$[μ_2-Pt(CN)$_4$]$_4$}$^{6-}$ fragment with the transition energy (E), wavelength λ, oscillator strength (f) and the excited state; description in terms of transitions between occupied and virtual NTOs (SAOP results).

E / cm^{-1}	λ / nm	f	State	NTO→NTO transitions			
				%	Spin	occupied	→ virtual
8670	1153	0.0002	1^7A	100	β	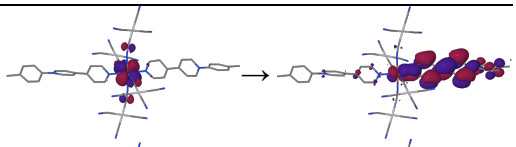	
9294	1076	0.0014	2^7A	100	α	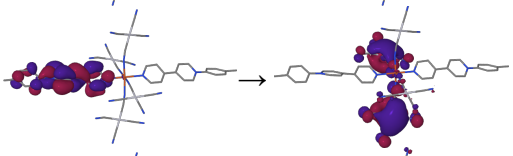	
9572	1045	0.0001	3^7A	100	α	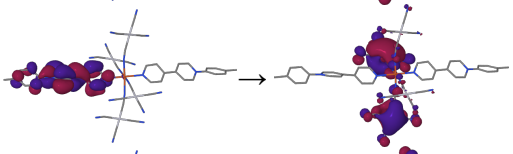	
10430	959	0.0006	4^7A	100	α	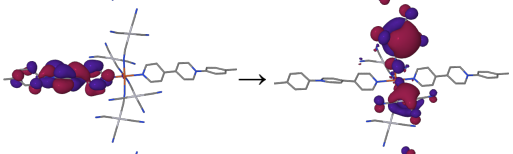	
10894	918	0.0002	5^7A	100	α	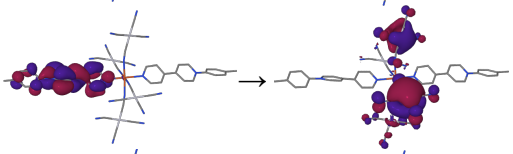	
11513	869	0.0019	6^7A	100	α	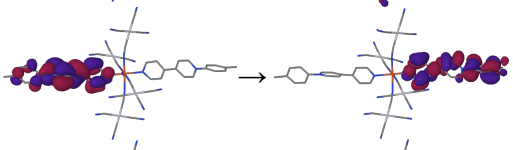	
11741	852	0.0000	7^7A	100	β	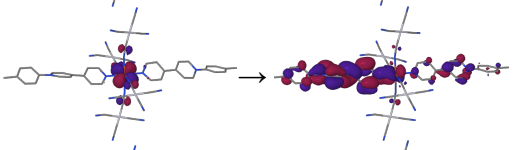	
11890	841	0.0004	8^7A	100	α	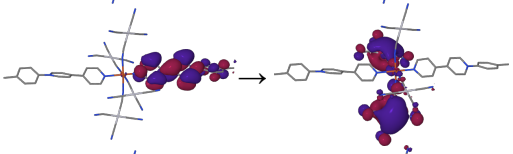	
12174	821	0.0009	9^7A	100	α	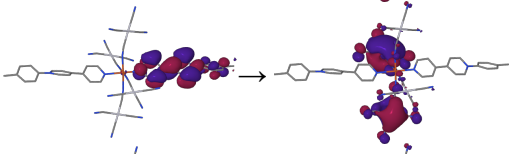	
12283	814	0.0003	10^7A	100	β	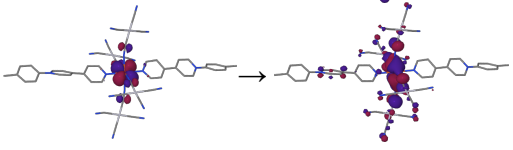	

12560	796	0.3584	11^7A	98	α	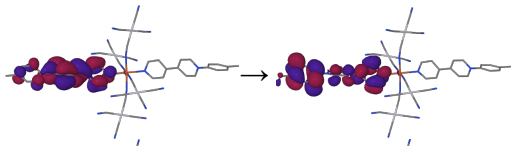
12833	779	0.0001	12^7A	100	α	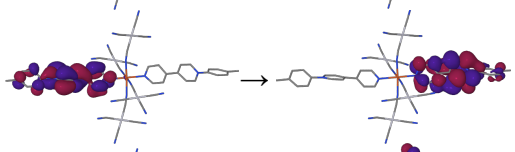
13037	767	0.0037	13^7A	100	α	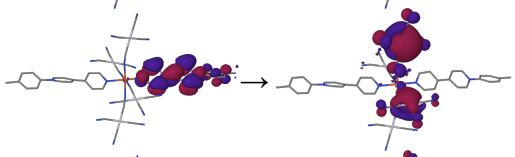
13492	741	0.0002	14^7A	100	α	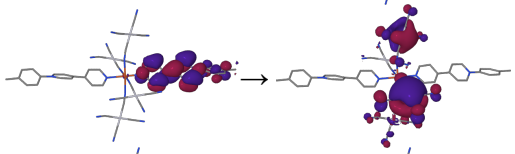
13891	720	0.0174	15^7A	97	α	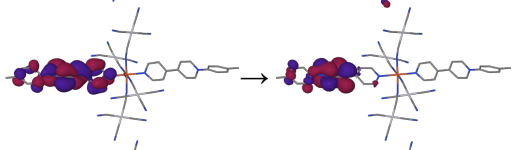
13900	719	0.0001	16^7A	98	α	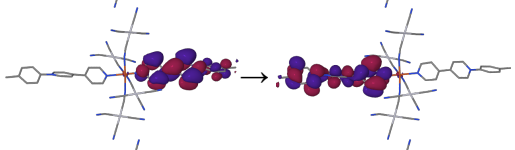
14839	674	0.0001	17^7A	99	β	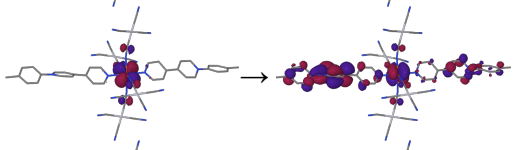
14970	668	0.0820	18^7A	96	α	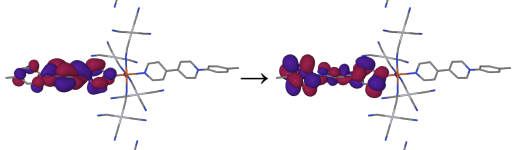
15092	663	0.4454	19^7A	95	α	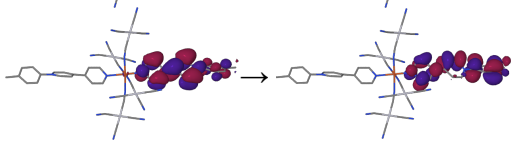
15327	652	0.0002	20^7A	100	α	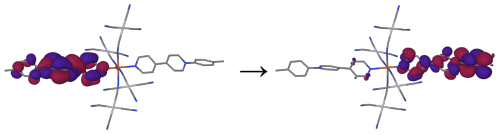
15460	647	0.0215	21^7A	100	α	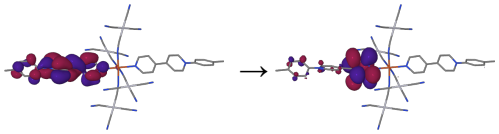
15739	635	0.0542	22^7A	99	α	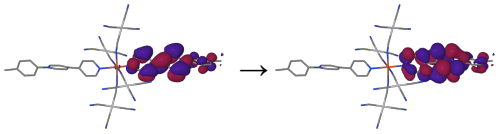

16049	623	0.0000	23^7A	100	α	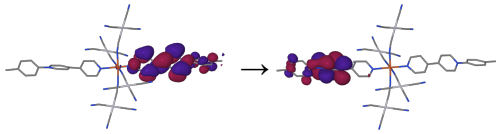
16471	607	0.0002	24^7A	100	α	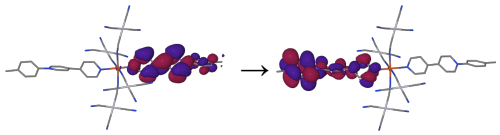
17574	569	0.0000	25^7A	100	α	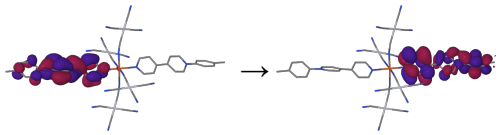
17890	559	0.0000	26^7A	100	α	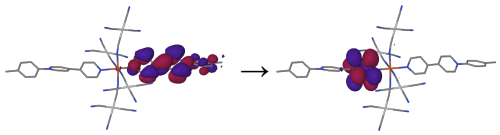
18257	548	0.0000	27^7A	100	α	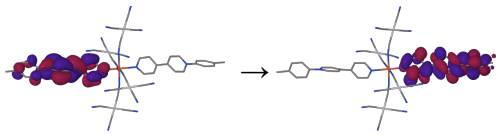
18567	539	0.0015	28^7A	100	α	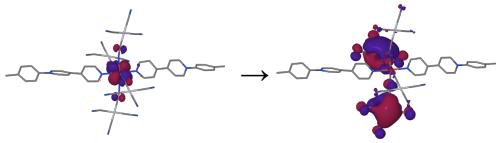
18668	536	0.0956	29^7A	100	β	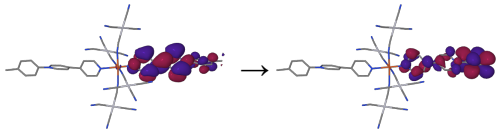
19077	524	0.0039	30^7A	100	β	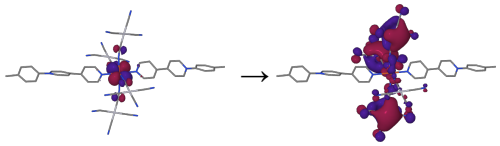

4 Supplementary Tables

4.1 Single Crystal X-Ray Diffraction

For single crystal XRD, the crystals were kept in their mother liquor until they were dipped into perfluoropolyether oil and their structure was determined. The chosen crystals were mounted on a Mitegen micromount. Data were collected at different temperatures (from 100 K to 300 K) on a XtaLAB Synergy (Rigaku) diffractometer using either a Cu-Kα radiation (λ = 1.54184 Å) or a Mo-Kα radiation (λ = 0.71073 Å) micro-source, equipped with an Oxford Cryosystems Cooler Device. The structures have been solved using the new dual-space algorithm program SHELXT [8] and refined by means of least-squares procedures using SHELXL-2018[8] program included either in the software package WinGX [9] version 1.639 or the package OLEX2 [10]. The Atomic Scattering Factors were taken from International Tables for X-Ray Crystallography [11]. Hydrogen atoms were placed geometrically and refined using a riding model, except for the hydrogens of water molecules which were located by Fourier Differences. All non-hydrogen atoms were anisotropically refined. Ellipsoid plots in the figures of the crystallography section were generated using the software ORTEP-3 [12]. The crystal structures have been deposited at the Cambridge Crystallographic Data Centre and allocated the deposition numbers 2321396-2321412, 2327738, 2327739 and 2355273.

Supplementary Table 9: Selected temperatures for {Fe(**CH_3-pbpy$^+$**)$_2$[μ_2-Pt(CN)$_4$]$_2$·2H_2O}; measurements were done from 150 to 290 K every 10 K.

Temperature, K	150(2)	200(2)	210(2)	250(2)	270(2)
formula	$C_{42}H_{30}N_{12}Pt_2Fe \cdot 2H_2O$				
fw, g/mol	1184.82	1184.82	1184.82	1184.82	1184.82
crystal size, mm	0.4x0.4x0.1	0.4x0.4x0.1	0.4x0.4x0.1	0.4x0.4x0.1	0.4x0.4x0.1
crystal colour	orange	orange	orange	orange	orange
crystal system	monoclinic	monoclinic	monoclinic	monoclinic	monoclinic
space group, *Z*	*P21/c*, 4	*P21/c*, 4	*P21/c*, 4	*P21/c*, 4	*P21/c*, 4
a, Å,	20.8823(3)	20.8921(2)	20.8823(3)	20.8819(2)	20.8823(3)
b, Å	12.9944(2)	13.05940(10)	12.9944(2)	13.12160(10)	12.9944(2)
c, Å	15.2591(2)	15.60910(10)	15.2591(2)	15.85790(10)	15.2591(2)
α, º	90	90	90	90	90
β, º	93.746(2)	93.2780(10)	93.746(2)	92.8690(10)	93.746(2)
*γ*º	90	90	90	90	90
V, Å^3	4131.75(10)	4251.79(6)	4131.75(10)	4339.68(6)	4131.75(10)
ρ, g/cm^3	1.905	1.851	1.905	1.813	1.905
μ, mm^{-1}	15.614	15.173	15.614	14.866	15.614
F(000)	2272	2272	2272	2272	2272
θ max, º	77.041	76.754	77.041	76.594	77.041
limiting indices	-26⇒h⇒26 -16⇒k⇒7 -18⇒l⇒19	-26⇒h⇒26 -16⇒k⇒7 -19⇒l⇒19	-26⇒h⇒26 -16⇒k⇒7 -18⇒l⇒19	-26⇒h⇒26 -16⇒k⇒7 -19⇒l⇒20	-26⇒h⇒26 -16⇒k⇒7 -18⇒l⇒19
reflections collected	8363	8588	8363	8724	8363
R_{int}	0.0615	0.0387	0.0615	0.0381	0.0615
data/parameters	7573/581	7822/581	7573/581	7617/581	7573/581
GOF on F^2	1.099	1.037	1.099	1.059	1.099
R_1 [I > 2σ(I)]	0.0605	0.0345	0.0605	0.0364	0.0605
R_1 (all data)	0.0658	0.0378	0.0658	0.0427	0.0658
wR_2 (all data)	0.1826	0.0974	0.1826	0.0997	0.1826
completness to theta max	95.5 %	95.6 %	95.5 %	95.3 %	95.5 %
lrgst diff peak, e/Å^3	3.49	1.65	3.49	0.93	3.49
lrgst diff hole, e/Å^3	-3.59	-1.01	-3.59	-1.18	-3.59

Supplementary Table 10: {Fe(**Br-pbpy$^+$**)$_2$[μ$_2$-Pt(CN)$_4$]$_2$·2H$_2$O}.

Temperature, K	100(2)	300(2)
formula	$C_{40}H_{24}Br_2N_{12}Pt_2Fe \cdot 2H_2O$	
fw, g/mol	1314.56	1314.56
crystal size, mm	0.4x0.4x0.1	0.4x0.4x0.1
crystal colour	orange	orange
crystal system	monoclinic	monoclinic
space group, *Z*	*P21/c*, 4	*P21/c*, 4
a, Å,	21.1504(2)	21.1717(3)
b, Å	12.97260(10)	13.2584(2)
c, Å	15.22460(10)	15.7335(2)
α, º	90	90
β, º	93.1490(10)	91.7430(10)
*γ*º	90	90
V, Å^3	4170.95(6)	4414.39(11)
ρ, g/cm^3	2.132	2.026
μ, mm^{-1}	17.730	16.791
F(000)	2528	2544
θ max, º	77.370	77.383
limiting indices	-26⇒h⇒25 -16⇒k⇒13 -19⇒l⇒17	-25⇒h⇒26 -16⇒k⇒-15 -19⇒l⇒18
reflections collected	8098	8411
R_{int}	0.0395	0.0505
data/parameters	7961/545	7401/545
GOF on F^2	1.140	1.040
R_1 [I > 2σ(I)]	0.0415	0.0456
R_1 (all data)	0.0420	0.0519
wR_2 (all data)	0.1142	0.1397
completness to theta max	99.8 %	97.7 %
lrgst diff peak, e/Å^3	2.82	1.56
lrgst diff hole, e/Å^3	-1.32	-1.86

Supplementary Table 11: {Zn(**Br-pbpy$^+$**)$_2$[μ_2-Pt(CN)$_4$]$_2$·2H$_2$O}.

Temperature, K	300(2)
formula	$C_{40}H_{24}Br_2N_{12}Pt_2Zn·2(H_2O)$
fw, g/mol	1324.11
crystal size, mm	0.15 × 0.15 × 0.03
crystal colour	colourless
crystal system	monoclinic
space group, *Z*	*P21/c*, 4
a, Å,	21.2020(1)
b, Å	13.2285(1)
c, Å	15.7562(1)
α, º	90
β, º	92.096(1)
*γ*º	90
V, Å^3	4419.53(5)
ρ, g/cm^3	1.990
μ, mm^{-1}	14.75
F(000)	2496
θ max, º	66.6°
limiting indices	−25⇒h⇒25 −15⇒k⇒14 −17⇒l⇒18
reflections collected	66584
R_{int}	0.054
data/parameters	7812/532
GOF on F^2	1.11
R_1 [I > 2σ(I)]	0.032
R_1 (all data)	0.0337
wR_2 (all data)	0.084
completness to theta max	1.000
lrgst diff peak, e/Å^3	1.48
lrgst diff hole, e/Å^3	−1.39

Supplementary Table 12: Fe(**$COOCH_3$-pbpy$^+$**)$_2$[μ_2-Pt(CN)$_4$]$_2$·2H_2O}.

Temperature, K	100(2)	300(2)
formula	$C_{44}H_{30}FeN_{12}O_4Pt_2 \cdot 2H_2O$	
fw, g/mol	1236.81	1236.81
crystal size, mm	0.15 × 0.12 × 0.03	0.15 × 0.12 × 0.03
crystal colour	red	pink
crystal system	Monoclinic	Monoclinic
space group, *Z*	*P21/n*, 2	*P21/n*, 2
a, Å,	11.6023(4)	12.0484(5)
b, Å	14.4285(4)	14.6058(5)
c, Å	14.1552(4)	14.0583(5)
α, º	90	90
β, º	110.535(3)	111.665(4)
*γ*º	90	90
V, Å^3	2219.06(12)	2299.17(16)
ρ, g/cm^3	1.911	1.844
μ, mm^{-1}	14.66	14.15
F(000)	1224	1232
θ max, º	65.1	65.1
limiting indices	−14⇒h⇒14 −14⇒k⇒17 −17⇒l⇒17	−15⇒h⇒15 −15⇒k⇒18 −17⇒l⇒17
reflections collected	37346	3921
R_{int}	0.047	0.059
data/parameters	3784/277	3921/287
GOF on F^2	1.08	1.12
R_1 [I > 2σ(I)]	0.054	0.050
R_1 (all data)	0.0575	0.0527
wR_2 (all data)	0.124	0.131
completness to theta max	0.999	0.999
lrgst diff peak, e/Å^3	1.77	1.66
lrgst diff hole, e/Å^3	−1.24	−1.37

5 Supplementary References

[1] (a) G. te Velde, F.M. Bickelhaupt, E.J. Baerends, C. Fonseca Guerra, S.J.A. van Gisbergen, J.G. Snijders and T. Ziegler, *Chemistry with ADF*, *J. Comput. Chem.* **22**, 931 (2001). DOI:10.1002/jcc.1056. (b) ADF 2021, SCM, Theoretical Chemistry, Vrije Universiteit, Amsterdam, The Netherlands, http://www.scm.com. Authors and contributors: E.J. Baerends, T. Ziegler, A.J. Atkins, J. Autschbach, O. Baseggio, D. Bashford, A. Bérces, F.M. Bickelhaupt, C. Bo, P.M. Boerrigter, C. Cappelli, L. Cavallo, C. Daul, D.P. Chong, D.V. Chulhai, L. Deng, R.M. Dickson, J.M. Dieterich, F. Egidi, D.E. Ellis, M. van Faassen, L. Fan, T.H. Fischer, A. Förster, C. Fonseca Guerra, M. Franchini, A. Ghysels, A. Giammona, S.J.A. van Gisbergen, A. Goez, A.W. Götz, J.A. Groeneveld, O.V. Gritsenko, M. Grüning, S. Gusarov, F.E. Harris, P. van den Hoek, Z. Hu, C.R. Jacob, H. Jacobsen, L. Jensen, L. Joubert, J.W. Kaminski, G. van Kessel, C. König, F. Kootstra, A. Kovalenko, M.V. Krykunov, P. Lafiosca, E. van Lenthe, D.A. McCormack, M. Medves, A. Michalak, M. Mitoraj, S.M. Morton, J. Neugebauer, V.P. Nicu, L. Noodleman, V.P. Osinga, S. Patchkovskii, M. Pavanello, C.A. Peeples, P.H.T. Philipsen, D. Post, C.C. Pye, H. Ramanantoanina, P. Ramos, W. Ravenek, M. Reimann, J.I. Rodríguez, P. Ros, R. Rüger, P.R.T. Schipper, D. Schlüns, H. van Schoot, G. Schreckenbach, J.S. Seldenthuis, M. Seth, J.G. Snijders, M. Solà, M. Stener, M. Swart, D. Swerhone, V. Tognetti, G. te Velde, P. Vernooijs, L. Versluis, L. Visscher, O. Visser, F. Wang, T.A. Wesolowski, E.M. van Wezenbeek, G. Wiesenekker, S.K. Wolff, T.K. Woo, A.L. Yakovlev

[2] (a) E. van Lenthe, E.J. Baerends and J.G. Snijders, *Relativistic regular two-component Hamiltonians*, *J. Chem. Phys.* **99**, 4597 (1993); DOI: 10.1063/1.466059 (b) A. Rosa, E.J. Baerends, S.J.A. van Gisbergen, E. van Lenthe, J.A. Groeneveld and J. G. Snijders, *Article Electronic Spectra of $M(CO)_6$ (M = Cr, Mo, W) Revisited by a Relativistic TDDFT Approach*, *J. Am. Chem. Soc.* **121**, 10356 (1999); DOI: 10.1021/ja990747t

[3] E. van Lenthe and E.J. Baerends, *Optimized Slater-type basis sets for the elements 1-118*, *J. Comput. Chem.* **24**, 1142 (2003); DOI: 10.1002/jcc.10255

[4] C.C. Pye and T. Ziegler, *An implementation of the conductor-like screening model of solvation within the Amsterdam density functional package*, *Theor. Chem. Acc.* **101**, 396 (1999); DOI: 10.1007/s002140050457

[5] (a) M. E. Casida, Time-dependent density functional response theory for molecules, in: D. P. Chong (Ed.), *Recent Advances in Density Functional Methods*, Vol. 1, World Scientific, Singapore, 1995, pp. 155–192. (b) S.J.A. van Gisbergen, J.G. Snijders and E.J. Baerends, *Implementation of time-dependent density functional response equations,* Comput. Phys. Commun. ***118**, 119 (1999); DOI: 10.1016/S0010-4655(99)00187-3*

[6] S. Hirata and M. Head-Gordon, *Time-dependent density functional theory within the Tamm-Dancoff approximation*, *Chem. Phys. Lett.* **314**, 291 (1999); DOI: 10.1016/S0009-2614(99)01149-5

[7] R.L. Martin, *Natural transition orbitals*, *J. Chem. Phys.* 118, 4775 (2003); DOI: 10.1063/1.1558471

[8] G. M. Sheldrick, Acta Cryst A 2015, 71, 3–8.

[9] L. J. Farrugia, J. Appl. Cryst. 1999, 32, 837–838.

[10] Olex2 1.5 (Dolomanov et al., 2009)

[11] INTERNATIONAL tables for X-Ray crystallography, 1974, Vol IV, Kynoch press, Birmingham, England.

[12] ORTEP3 for Windows - L. J. Farrugia, J. Appl. Crystallogr. 1997, 30, 565.